Paleoceanography and Paleoclimatology

RESEARCH ARTICLE
10.1029/2022PA004555

Special Section:
Illuminating a Warmer World: Insights from the Paleogene

North Atlantic Drift Sediments Constrain Eocene Tidal Dissipation and the Evolution of the Earth-Moon System

David De Vleeschouwer[1,2], Donald E. Penman[3], Simon D'haenens[4,5,6], Fei Wu[7], Thomas Westerhold[2], Maximilian Vahlenkamp[2], Carlotta Cappelli[8], Claudia Agnini[8], Wendy E. C. Kordesch[9], Daniel J. King[10], Robin van der Ploeg[11,12], Heiko Pälike[2], Sandra Kirtland Turner[13], Paul Wilson[14], Richard D. Norris[15], James C. Zachos[16], Steven M. Bohaty[14,17], and Pincelli M. Hull[4]

[1]Institute of Geology and Palaeontology, University of Münster, Münster, Germany, [2]MARUM - Center for Marine Environmental Sciences, University of Bremen, Bremen, Germany, [3]Department of Geosciences, Utah State University, Logan, UT, USA, [4]Department of Earth and Planetary Sciences, Yale University, New Haven, CT, USA, [5]Research Coordination Office, Hasselt University, Hasselt, Belgium, [6]Data Science Institute, Diepenbeek, Belgium, [7]School of Earth Sciences, State Key Laboratory of Geological Processes and Mineral Resources, China University of Geosciences, Wuhan, China, [8]Dipartimento di Geoscienze, Università di Padova, Padova, Italy, [9]Greater Farallones Association, San Francisco, CA, USA, [10]School of Geography, Environment, and Earth Sciences, Victoria University of Wellington, Wellington, New Zealand, [11]Department of Earth Sciences, Utrecht University, Utrecht, The Netherlands, [12]Shell Global Solutions International B.V., Amsterdam, The Netherlands, [13]Department of Earth and Planetary Sciences, University of California – Riverside, Riverside, CA, USA, [14]Ocean and Earth Science, University of Southampton, National Oceanography Centre, Southampton, UK, [15]Center for Marine Biodiversity and Conservation, Scripps Institution of Oceanography, University of California San Diego, La Jolla, CA, USA, [16]Department of Earth & Planetary Science, University of California, Santa Cruz, CA, USA, [17]Institute of Earth Sciences, Heidelberg University, Heidelberg, Germany

Key Points:

- A new precession-based cyclostratigraphy for the middle Eocene intervals of IODP Sites U1408 and U1410
- Variability in astronomical fundamental frequencies (g-terms) on million-year timescales is larger than previously assumed
- Our precession constant estimate for 41 Ma (51.28 ± 0.56″/year) confirms earlier indicators of slower tidal dissipation in the Paleogene

Correspondence to:
D. De Vleeschouwer,
ddevlees@uni-muenster.de

Citation:
De Vleeschouwer, D., Penman, D. E., D'haenens, S., Wu, F., Westerhold, T., Vahlenkamp, M., et al. (2023). North Atlantic drift sediments constrain Eocene tidal dissipation and the evolution of the Earth-Moon system. *Paleoceanography and Paleoclimatology*, *38*, e2022PA004555. https://doi.org/10.1029/2022PA004555

Received 16 SEP 2022
Accepted 11 JAN 2023

Abstract Cyclostratigraphy and astrochronology are now at the forefront of geologic timekeeping. While this technique heavily relies on the accuracy of astronomical calculations, solar system chaos limits how far back astronomical calculations can be performed with confidence. High-resolution paleoclimate records with Milankovitch imprints now allow reversing the traditional cyclostratigraphic approach: Middle Eocene drift sediments from Newfoundland Ridge are well-suited for this purpose, due to high sedimentation rates and distinct lithological cycles. Per contra, the stratigraphies of Integrated Ocean Drilling Program Sites U1408–U1410 are highly complex with several hiatuses. Here, we built a two-site composite and constructed a conservative age-depth model to provide a reliable chronology for this rhythmic, highly resolved (<1 kyr) sedimentary archive. Astronomical components (g-terms and precession constant) are extracted from proxy time-series using two different techniques, producing consistent results. We find astronomical frequencies up to 4% lower than reported in astronomical solution La04. This solution, however, was smoothed over 20-Myr intervals, and our results therefore provide constraints on g-term variability on shorter, million-year timescales. We also report first evidence that the g_4–g_3 "grand eccentricity cycle" may have had a 1.2-Myr period around 41 Ma, contrary to its 2.4-Myr periodicity today. Our median precession constant estimate (51.28 ± 0.56″/year) confirms earlier indicators of a relatively low rate of tidal dissipation in the Paleogene. Newfoundland Ridge drift sediments thus enable a reliable reconstruction of astronomical components at the limit of validity of current astronomical calculations, extracted from geologic data, providing a new target for the next generation of astronomical calculations.

Plain Language Summary The traditional cyclostratigraphic approach is to align and correlate a geologic depth-series with an astronomical solution. However, the chaotic nature of the Solar System prevents astronomers from precisely calculating planetary motions beyond 40–50 million years ago. This in turn limits the options for geologists to use the resulting oscillations in Earth's climate system as a metronome for determining geologic time. In this study, we reversed the cyclostratigraphic approach and used the highly rhythmical sedimentary deposits from Newfoundland Ridge (North Atlantic) to back-calculate planetary motions at ~41 million years ago. The superior quality of the Newfoundland Ridge geoarchive originates from the combination of relatively high sedimentation rates (~4 cm/kyr) and the time-continuous character of our two-site composite record between 39.5 and 42.8 million years ago. In this work, we had to first overcome considerable challenges in reconstructing the timing of sediment deposition, which we did with highly resolved geochemical measurements from two sites. We then were able to extract information on the Earth's planetary

motion and on the Earth-Moon interactions. These astronomical reconstructions based on geological data can now be used by astronomers to describe the evolution of the solar system further back in time than was previously possible.

1. Introduction

Accurate and highly resolved age models are necessary for unraveling causal relationships in paleoclimatology. For this reason, cyclostratigraphy and astrochronology became indispensable tools over the last few decades. However, astrochronologies crucially depend on reliable orbital calculations of Solar System dynamics far back in time (Sinnesael et al., 2019). Variations in Earth's astronomical parameters of eccentricity, obliquity and precession significantly alter the distribution and amount of incoming solar radiation in space and time (Laskar et al., 2004; Milanković, 1941). Following Quinn et al. (1991), recent orbital models of the Solar System are constructed by direct numerical integration (Laskar et al., 2004, Laskar et al., 2011a; Laskar, Gastineau, et al., 2011; Varadi et al., 2003; Zeebe, 2017; Zeebe & Lourens, 2019). These numerical integrations describe the orientation and shape of the orbital bodies considered, and can be characterized by a set of fundamental frequencies that describe the motion of orbits within, and perpendicular to their orbital planes (the so-called g_i terms or eccentricity modulation terms, and s_i terms or orbital inclination terms, respectively) (Pälike, 2005). Each of those frequencies is associated with the particular orbital movement of one of the nine (dwarf) planets in the Solar system (the "i" index), whereby $i = 1$ refers to Mercury and $i = 9$ to Pluto. These fundamental frequencies change slowly on million-year time scales (Laskar, 1990) and are therefore denoted "secular terms". To date, our knowledge on the variability and trends of these terms comes almost exclusively from astronomical models, and first attempts to reverse the cyclostratigraphic approach indicate that the past variability of these terms could have been greater than previously thought (Meyers & Malinverno, 2018). Moreover, the orbital calculations also exhibit chaotic behavior (Laskar, 1990) and a fuller characterization of the orbital system must involve resonant and non-linear terms. More recent orbital calculations that also include major asteroids like Ceres and Vesta (Laskar, Gastineau, et al., 2011c; Zeebe, 2017) have shown that the chaotic evolution of the solar system limits the time span for which valid calculations can be made of Earth's eccentricity and orbital inclination to around 60 Ma in the most optimistic case. However, different solutions diverge significantly beyond ~48 Ma. Several other uncertainties, like, for example, the J2 quadrupole moment of the Sun (Laskar, 1999; Laskar et al., 2004; Zeebe & Lourens, 2019), further indicate that orbital solutions must be constrained by geological observations.

Certain orbital amplitude modulation terms have been shown to be stable over long periods of time. These so-called astronomical metronomes can be used as a framework to construct detailed cyclostratigraphies in deep time. The 405-kyr long eccentricity term (g_2–g_5), for example, has been shown to be stable beyond 60 Ma (Kent et al., 2018; Olsen et al., 2019). Likewise, the s_3–s_6 orbital inclination term (~173-kyr obliquity amplitude modulator) is still phase coherent between different orbital integrations back to 48 Ma (Boulila et al., 2018). While the above discussion relates to the orbital components, Earth's climatic precession and obliquity evolution also involves the precession frequency of the Earth p, which is influenced by the distribution of angular momentum within the Earth-Moon system. Tidal friction steadily slows the Earth's rotational speed, among other effects. To maintain angular momentum within the Earth-Moon system, the Earth-Moon distance increases as an immediate consequence. This effect results in a decrease of the precession frequency p over time and, therefore, in a progressive decline in the main frequency components of Earth's obliquity ($p + s_{1–4}$ and $p + s_6$ terms) and precession ($p + g_{1–5}$) periodicities. The current rate at which rotational energy dissipates is, however, a poor guide for the past. Present-day tidal dissipation would imply zero Earth-Moon distance at ~1.5 Ga, whereas the Moon is ~4.5 Gyr old (Green et al., 2017; Hansen, 1982; Waltham, 2015). While it is generally accepted that tidal dissipation must have been lower throughout much of Earth history, uncertainties on its temporal evolution remain (Daher et al., 2021). This ambiguity also holds for geologic Epochs as recent as the Eocene: Color reflectance (a*b*) data from Walvis Ridge ODP Site 1262 has been used both by Meyers and Malinverno (2018) and Zeebe and Lourens (2022) to reconstruct tidal dissipation around 55 Ma. Their approaches are very different, but both studies adopt iterative data-model fitting approaches that simultaneously derive floating age-depth models and the precession frequency p. Both teams likewise firmly conclude that early Eocene tidal dissipation must have been lower than the present-day value, but caution that more precise tidal dissipation reconstructions require independent age-depth model constraints. Thus, the lingering uncertainty on early Cenozoic tidal dissipation limits accurate insolation reconstructions to the Neogene (Lourens et al., 2001; Pälike & Shackleton, 2000; Zeeden

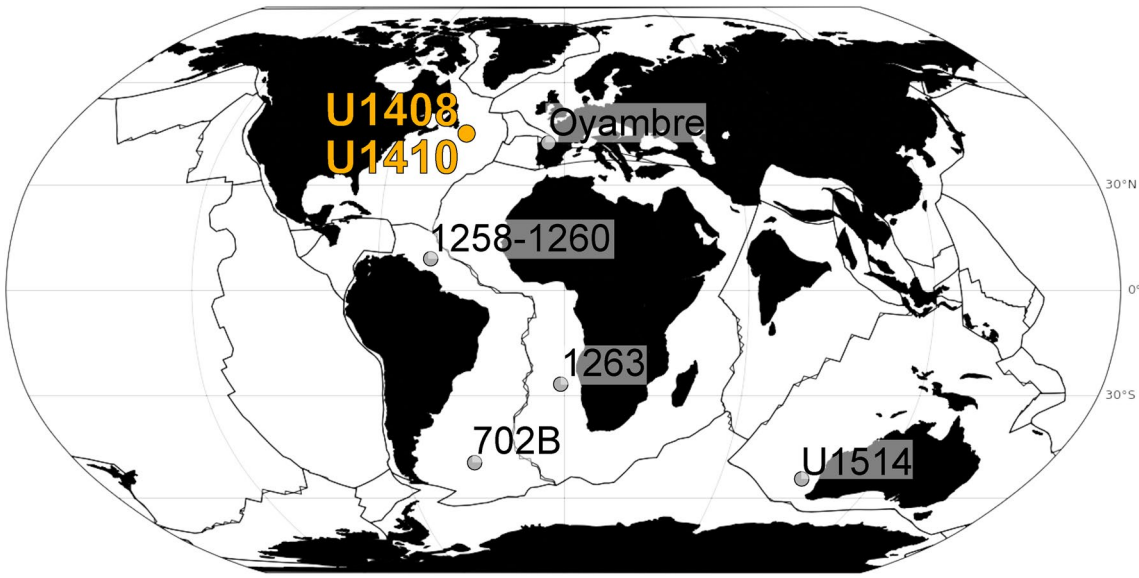

Figure 1. Paleogeographic map with existing cyclostratigraphies for the Middle Eocene. The location of studied IODP sites U1408 and U1410 is indicated in orange. Other cyclostratigraphies refer to Dinarès-Turell et al. (2018), Westerhold and Röhl (2013), Westerhold et al. (2014), Westerhold et al. (2015), and Vahlenkamp et al. (2020). Map made with GPlates (Müller et al., 2018) using the paleomagnetic reference frame of Matthews et al. (2016).

et al., 2014). To move forward, orbital terms extracted from accurately dated geological archives are now required to benchmark astronomical solutions regarding the evolution of the solar system.

The middle Eocene is a time of gradual global cooling, interrupted by a remarkable warm event called the Middle Eocene Climatic Optimum (MECO) (Bohaty & Zachos, 2003; Bohaty et al., 2009). The MECO is marked by large temperature, sea level and salinity variations in the North Atlantic, the Arctic Ocean and the North Sea (e.g., Cramwinckel et al., 2020; Marchegiano & John, 2022; van der Ploeg et al., 2023). The contourite drift deposit sequences of International Ocean Discovery Program (IODP) Site U1408 and Site U1410 (Newfoundland Ridge, North Atlantic, IODP Expedition 342, Figure 1) provide a high-resolution paleoceanographic archive throughout this time interval and have the potential to supply a test for Earth-Moon dynamics and the evolution of the solar system. The onset of contourite deposition occurred at both sites around 47 Ma, when an order-of-magnitude increase in terrigenous mass accumulation rate resulted in high overall sedimentation rates (>2 cm/kyr) (Boyle et al., 2017; Cappelli et al., 2019) and a sedimentary system sensitive to astronomical insolation forcing (Vahlenkamp et al., 2018). Post-expedition, the science team collaborated to obtain cm-resolution benthic isotope data, as well as X-Ray Fluorescence (XRF) core scans for this unique Eocene sedimentary archive. However, the utility of this multi-proxy data set has been limited by problems related to obtaining a reliable composite depth- and time-scales, which in turn are due to complicated drift sediment lithologies at IODP Sites U1408 and U1410 (Boulila et al., 2018; Boulila & Hinnov, 2022; Cappelli et al., 2019; Vahlenkamp et al., 2018; Zeebe & Lourens, 2022). Hence, the first task for this study is to resolve the U1408– U1410 middle Eocene time-scale controversies. This is achieved by integrating high-resolution benthic foraminiferal stable isotope records (N = 3,424) and X-ray Fluorescence (XRF) derived elemental ratios (N = 9,662) into a new two-site composite section and a robust stratigraphic framework that acknowledges the fragmentary nature of the individual IODP Sites. With a revised and improved chronostratigraphic framework, these geochemical records provide the means to attain the second objective of extracting information on the long-term chaotic evolution of the solar system.

2. Materials and Methods

2.1. Lithologic Description

A middle Eocene two-site composite record forms the backbone of this study. The composite consists of IODP Site U1408 (41°26.30'N, 49°47.10'W, 3,022 m water depth) and Site U1410 (41°19.69'N, 49°10.18'W, 3,400 m water depth), which were both cored on the Newfoundland Ridge (North Atlantic) during IODP Expedition 342 at

paleodepths of ~2,575 m and ~2,950 m, respectively (Norris et al., 2014). The middle Eocene sequences archive a record of cyclical environmental change, characterized by the unique combination of rhythmic, lithologic alternations of greenish nannofossil-rich clay and whitish nannofossil ooze, high sedimentation rates (2–5 cm/kyr), well-defined magnetostratigraphic boundaries (uncertainties ≤ ±1m) (Boulila et al., 2018), well-studied calcareous nannofossil biostratigraphy (Table 1) (Bown & Newsam, 2017; Cappelli et al., 2019; Newsam, 2016), and the availability of high-resolution XRF-derived and isotopic proxies.

2.2. X-Ray Fluoresence and Benthic Stable Isotope Proxies

XRF-derived Ca/Fe ratios were measured at 2-cm resolution at MARUM (University of Bremen) and the Scripps Institution of Oceanography (University of California San Diego) on Avaatech core scanners. The studied interval consists of 9,662 Ca/Fe data points in the final two-site composite. Stable carbon and oxygen isotopes of benthic foraminifera *Nuttallides truempyi* (2–6 shells per analysis) were measured at 3–6 cm resolution by a consortium consisting of MARUM (Bremen University), National Oceanography Center (Southampton), University of California (San Diego), the University of California (Santa Cruz), and Yale University (New Haven). In all labs, 20cc sediment samples were dried and then washed through a 63-µm sieve. Two to six individuals of *Nuttalides truempyi* were picked and run for stable carbon and oxygen isotopes using a Kiel IV carbonate preparation device coupled to a ThermoFisher MAT 253 Plus isotope ratio mass spectrometer, using established dual-inlet techniques. The studied interval consists of 3,424 data points in the final two-site composite. Benthic *Nuttallides truempyi* $\delta^{13}C$ and $\delta^{18}O$ values are converted to *Cibicidoides* for comparison with the CENOGRID reference curve (Westerhold et al., 2020), using the conversion factors of Katz et al. (2003): $\delta^{18}O_{Cib} = \left(\delta^{18}O_{Nut} + 0.1\right)/0.89$.

2.3. Extracting Astronomical Fundamental Frequencies and Precession Constant

2.3.1. Numerical Analysis of Fundamental Frequencies

Astronomical frequencies were extracted from the geological data using numerical analysis of fundamental frequencies (NAFF). NAFF performs high-resolution frequency analysis of time series as designed by Laskar (1990), and previously used by Olsen et al. (2019) to extract astronomical frequencies from a Triassic-Jurassic lake depth rank series. Here, we apply the NAFF technique to the log(Ca/Fe) time-series (39.47–42.81 Ma), as well as to the amplitude envelope of the precession cycles within the log(Ca/Fe) data (39.47–42.81 Ma), and to the benthic isotope time-series (39.47–40.82 Ma). The NAFF method has been implemented in a macOS command line tool by Pälike (2021b). The astrochron R package was used to calculate multi-taper method spectra, Taner bandpass filters and Hilbert transforms for amplitude envelope extraction (Meyers, 2014).

2.3.2. TimeOptMCMC

To verify the NAFF result, and to quantify the uncertainties in the extracted astronomical frequencies, we additionally applied the TimeOptMCMC method (Meyers & Malinverno, 2018) to the log(Ca/Fe) time-series (39.47–42.81 Ma). The TimeOptMCMC function is implemented in the *astrochron* R package (Meyers, 2014). Through Bayesian Markov Chain Monte Carlo simulations, different plausible combinations of the solar system secular frequencies g_1 to g_5 and the precession constant p are compared to the stratigraphic data, and their match is reformulated in terms of a likelihood function. For this study, we apply TimeOptMCMC to the log(Ca/Fe) time-series rather than the depth-series, yet we allowed for minor perturbations of our time-axis by ±10%. TimeOptMCMC was run twice: First, TimeOptMCMC is run with the same prior beliefs on g-term and precession constant averages as in the Eocene analysis in Meyers and Malinverno (2018). Second, TimeOptMCMC is run with updated prior beliefs, based on the NAFF results. Both analyses each consist of 106 Markov Chain Monte Carlo runs, each of which consists of 200,000 samples, sufficient to explore the entire parameter space. Every chain is characterized by a burn-in phase, during which the combinations of astronomical frequencies converge toward a high-probability region of the posterior probability density function. We determined the burn-in phase in the same way as Meyers and Malinverno (2018), first computing the median likelihood value in the second half of the chain and then defining the burn-in end as the first sample in the chain that reaches a likelihood value greater than this median value. Finally, we combine the results of the 106 independent chains to display posterior distributions.

2.3.3. Dynamical Ellipticity, Tidal Dissipation and the Precession Constant

The periods for precession and obliquity are known to have been shorter in the geologic past, compared to the present-day (Berger et al., 1992). This is the direct result of changes in the precession constant p, which appears

Table 1
Calcareous Nannofossil Biostratigraphic Datums and Magnetostratigraphic Datums in the IODP Site U1408-U1410 Middle Eocene Composite Section: B = Base, Bc = Base Continuous and Common, T = Top, Tc = Top Continuous and Common

	Species/Chronozone	Sample top	Sample base	Inter-site mapped depth (CCSF-X)			Age GTS2020 (Ma)	Age this study (Ma)	Source and visual depiction
				Top	Base	Mean			
B	C18n.1r	Averaged reversal depths in U1408B and U1408C		55.69	55.71	55.70	39.666	39.671	B18 and Fig. S14 in C19
Tc	*Sphenolithus spiniger*	U1408C 7H5, 93 cm	U1408C 7H5, 109 cm	59.72	59.88	59.80		39.81	N16
B	*Sphenolithus obtusus*	U1408B 8H3, 18 cm	U1408B 8H3, 49 cm	62.77	63.09	62.93		39.91	N16
B	C18n.2n	U1410B 10H5, 130 cm	U1410B 10H5, 130 cm	70.77	70.77	70.77	40.073	40.198	B18 and Fig. S14 in C19
T	*Chiasmolithus solitus*	U1408B 8H6, 33 cm	U1408B 8H6 64 cm	74.06	74.37	74.21	39.23	40.31	N16 and Fig. S14 in C19
B	*Reticulofenestra stavensis* or *Dictyococcites bisectus*	U1408A 8H2, 63 cm	U1408A 8H2, 79 cm	78.35	78.51	78.43	40.25	40.43	N16 and Fig. S14 in C19
Bc	*Sphenolithus predistentus*	U1408A 8H4, 108 cm	U1408A 8H4, 139 cm	81.80	82.11	82.95		40.52	N16
T	*Sphenolithus furcatolithoides*	U1408C 9H4, 93 cm	U1408C 9H4, 109 cm	85.55	85.71	85.63	40.39	40.58	N16 and Fig. S14 in C19
B	C18r	Averaged reversal depths in U1410A and U1410B		105.15	105.23	105.19	41.030	41.091	B18 and Fig. S15 in C19
B	C19n	Averaged reversal depths in U1410A, U1410B and U1410C		111.25	112.83	112.04	41.180	41.291	B18 and Fig. S16 in C19
B	C19r	Averaged reversal depths in U1408A and U1408B		133.98	134.16	134.07	42.196	42.181	B18 and Fig. S17 in C19
Bc	*Reticulofenestra umbilicus*	U1408C 13H6, 3 cm	U1408B 14H2, 124 cm	134.99	136.10	135.55	42.72	42.22	N16 and Fig. S17 in C19
T	*Nannotetrina fulgens*	U1408C 17H4, 3 cm	U1408B 18H2, 3 cm	171.80	173.33	172.56		43.30	N16 and Fig. S18 in C19
B	C20n	U1410B 18H4, 32 cm	U1410B 18H4, 46 cm	181.46	181.60	181.53	43.450	43.495	C19 and Fig. S17 in C19
T	*Pletolithus gigas*	U1410A 17X2, 80 cm	U1410B 19X 3, 40 cm	187.32	187.38	187.35	43.64	43.62	C19 and Fig. S18 in C19
Bc	*Spenolithus furcatolithoides*	U1410B 19X3, 40 cm	U1410A 17X2, 120 cm	187.38	187.72	187.55		43.62	C19 and Fig. S18 in C19
Tc	*Pletolithus gigas*	U1410B 19X6, 60 cm	U1410B 19X6, 80 cm	191.74	191.90	191.82		44.31	C19
T	*Pletolithus gigas*	U1408A 17H4, 3 cm	U1408B 20X5, 4 cm	192.12	201.78	196.95	43.64	44.42	N16 and Fig. S18 in C19
B	*Sphenolithus cuniculus*	U1410C 18X5, 20 cm	U1410C 18X5, 100 cm	201.23	202.03	201.63	44.40	44.53	C19
Bc	*Sphenolithus pseudofurcalolithoides*	U1410B 21X4, 127 cm	U1410B 21X5, 7 cm	215.17	215.47	215.32		45.14	C19
B	*Sphenolithus pseudofurcalolithoides*	U1410C 20X4, 67 cm	U1410C 20X4, 107 cm	223.73	224.16	223.95	45.87	45.59	C19 and Fig. S19 in C19
B	*Pletolithus gigas*	U1410A 20XCC, 36 cm	U1410C 21X5, 7 cm	229.97	231.93	230.95	46.07	45.71	C19 and Fig. S19 in C19

Table 1
Continued

	Species/Chronozone	Sample top	Sample base	Inter-site mapped depth (CCSF-X) Top	Base	Mean	Age GTS2020 (Ma)	Age this study (Ma)	Source and visual depiction
B	C20r	U1410A 21X6, 91 cm	U1410A 21X7, 63 cm	241.97	243.19	242.58	46.235	45.928	C19
B	*Nannotetrina alata* group	U1410B 24X1, 87 cm	U1410B 24X2, 87 cm	246.06	247.79	246.93	46.72	46.01	C19

Note. Data sources: N16 = Newsam (2016); B18 = Boulila et al. (2018); C19 = Cappelli et al. (2019). *S. pseudofurcalolithoides* was previously referred to as *S. furcatolithoides* morph A (Cappelli et al., 2021), while *Pletolithus gigas* was previously referred to as *Chiasmolithus gigas* (Cappelli et al., 2020).

in all precession ($p + g_i$) and obliquity ($p + s_i$) arguments. The precession constant p arises from the solution of the Poisson equation describing the Earth-Moon system, which is Equation 7 in Berger et al. (1992) and Equation 8 in Laskar et al. (2004). This equation entails both the rotational angular velocity of the Earth and the dynamical ellipticity of the Earth. Both parameters change slowly through geologic time. The rotational angular velocity of the Earth decreases due to tidal friction and other energy dissipative effects (e.g., core-mantle friction). The dynamical ellipticity of the Earth changes due to plate tectonics or the build-up of continental ice sheets. Several cyclostratigraphers have reconstructed tidal dissipation and dynamical ellipticity from Neogene geologic data without translating them to their respective precession constant p (Lourens et al., 2001; Pälike & Shackleton, 2000; Zeeden et al., 2014). We developed a Graphical User Interface (De Vleeschouwer, 2023) that approximates the effect of dynamical ellipticity and tidal dissipation on the precession constant p, using the formulation in Laskar et al. (1993) and assuming S_0 and ε_0 constant. The interface was used to translate the results of Pälike and Shackleton (2000), Lourens et al. (2001), and Zeeden et al. (2014) into a precession constant p value.

3. A Two-Site U1408–U1410 Composite

The middle Eocene drift deposit sequences of IODP Site U1408 and Site U1410 (Newfoundland Ridge, North Atlantic) consist of nannofossil clay marked by rhythmical alternations between more clay-rich and more nannofossil-rich endmembers. The clay-content variability occurs on the meter-scale (0.6–1.2 m) and was initially interpreted as obliquity-paced cyclicity (Boulila et al., 2018; Boulila & Hinnov, 2022; Vahlenkamp et al., 2018). However, a site-to-site correlation by Cappelli et al. (2019) revealed numerous hiatuses within the individual records, as well as splicing mistakes that doubled strata. The recovered middle Eocene sequences therefore represent less time than originally thought, and doubts emerged on the original astronomical interpretation. The suspicion arose that the lithological rhythm is reflecting precession rather than obliquity. The Cappelli et al. (2019) results basically represented a return to square one: A return to the depth-domain. Here, we combine the site-to-site correlation by Cappelli et al. (2019) (Figure 2) with our own additional stratigraphic interpretations (Figure 3) to come up with a two-site composite in the depth domain (Figure 4), maximizing stratigraphic completeness. We then convert the composite from depth-to-time and assess the hypothesis that the distinct lithological cycle in clay-content represents precession rather than obliquity.

The construction of the U1408–U1410 composite (called CCSF-X) is underpinned by an integrated stratigraphic approach, combining all available magneto-, bio- and chemostratigraphic information that constrains the two-site correlation in the depth-domain. While we were able to make a site-to-site correlation throughout the studied interval, we had to adopt a different composite-building strategy in the upper and lower part of the composite. In the upper part of the composite (*Bohaty composite* in Figure 4), the site-to-site correlation reveals up to 10-m-thick intervals that are present at one site but not at the other (Figure 3). Hence, the upper part of the composite is constructed by filling in gaps at one site with sections from the other. This approach results in a composite section that is significantly more expanded compared to the individual sites, and that is therefore closer to a continuous sedimentary representation of geologic time. In the lower part of the composite (*Cappelli composite* in Figure 4), the Cappelli et al. (2019) site-to-site correlation revealed that Site U1408 is the more complete record, with gaps and condensed intervals occurring more frequently at Site U1410. For that reason, Site U1410 was mapped onto the Site U1408 composite depth scale (Cappelli et al., 2019). In contrast to the upper part of the composite, Site

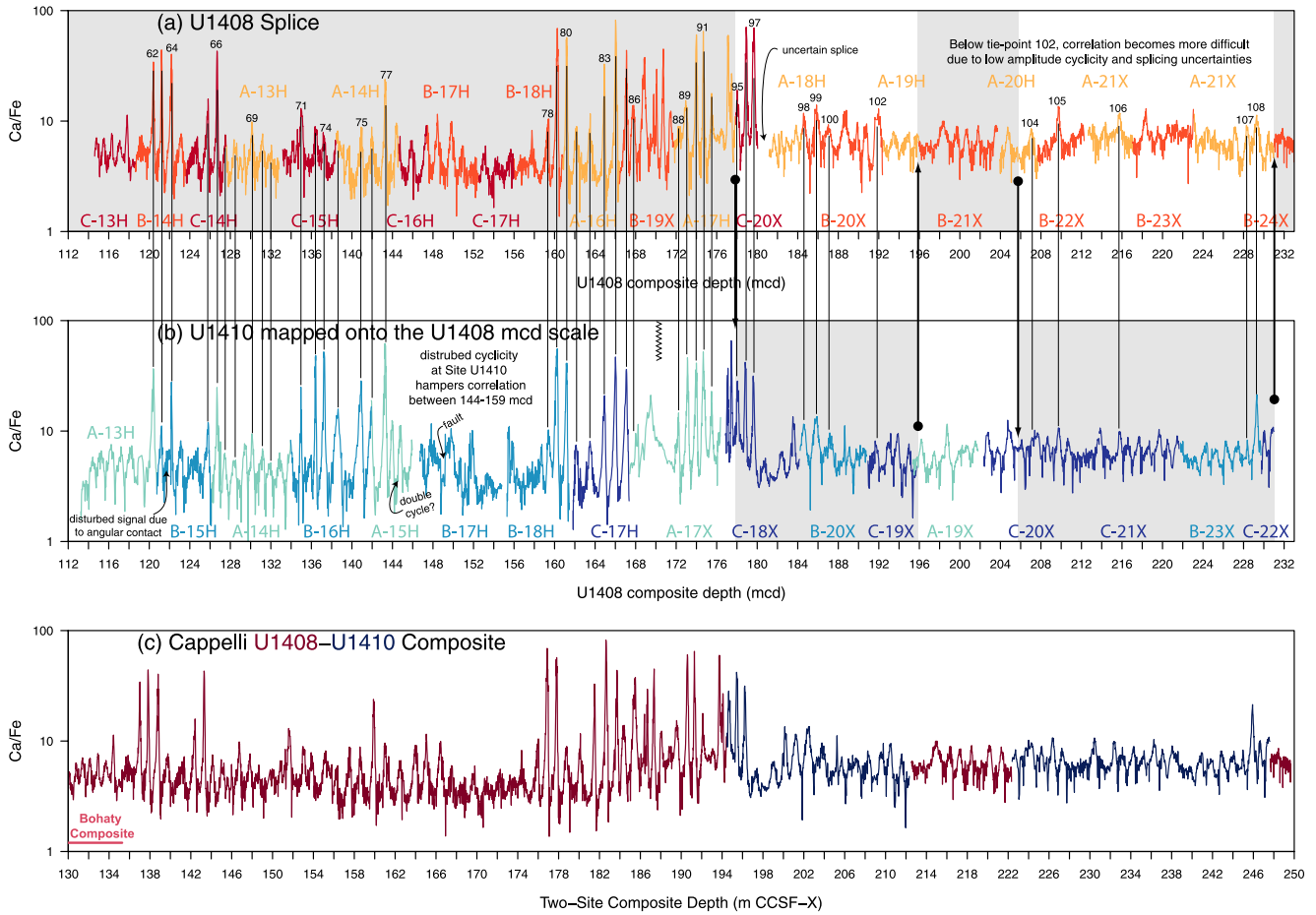

Figure 2. Construction of the lower *Cappelli* composite. Cappelli et al. (2019) correlated individual cycles between U1408 and U1410 and used them to map Site U1410 onto the U1408 depth scale. In contrast to Figure 3, all U1410 data are squeezed/stretched to accord with the U1408 depth scale. Hence, all correlation lines are straight. A composite record was then constructed, avoiding disturbed cyclicity, hiatuses, and splice uncertainties (Figure 4). This part of the composite is attached to the *Bohaty* composite (Figure 3) through Core U1408C-13H, which is incorporated within both composites.

U1410 does not contain any sections that can fill in for stratigraphic gaps at Site U1408. Obviously, this does not imply that Site U1408 is continuous. Instead, we suspect that there are missing cycles at Site U1408, which are also missing from Site U1410. We therefore infer that the lower composite is likely not time-continuous, in contrast to the upper part of the composite. Nevertheless, the site-to-site correlation in the lower composite provides long stretches of high-resolution stable isotope data (~1 kyr resolution) which may come in useful for a wide range of paleoceanographic investigations (Figure 2).

4. A Precessional Rhythm for the Middle Eocene Newfoundland Ridge Lithological Cycles

The conversion from depth to time consists of twenty tie-points (Figure 5). Linear interpolation is adopted in-between tie-points. The age-depth model was constructed by aligning the composite's isotope records with the CENOGRID stratigraphic backbone (Westerhold et al., 2020), while simultaneously aligning pronounced lithological cycles (i.e., high-amplitude Ca/Fe cycles) with eccentricity maxima in the La11 eccentricity solution (Laskar et al., 2011b), and by considering the available magneto- and biostratigraphic datums (Table 1). The age-depth model came about through a trial-and-error approach, until a satisfactory fit was achieved with as few age-depth tie-points as possible (Figure 6). This low number of tie-points is essential to avoid the importation of astronomical terms from CENOGRID or the La11 solution into the U1408/U1410 composite, and thus to avoid circular reasoning during the extraction of astronomical components from that composite. Tie-points are typically spaced several hundred thousand years apart (Figure 5), meaning there could only be an influence on the 405-kyr g_2–g_5 eccentricity term. This potential influence is considered acceptable since the g_2–g_5 term is

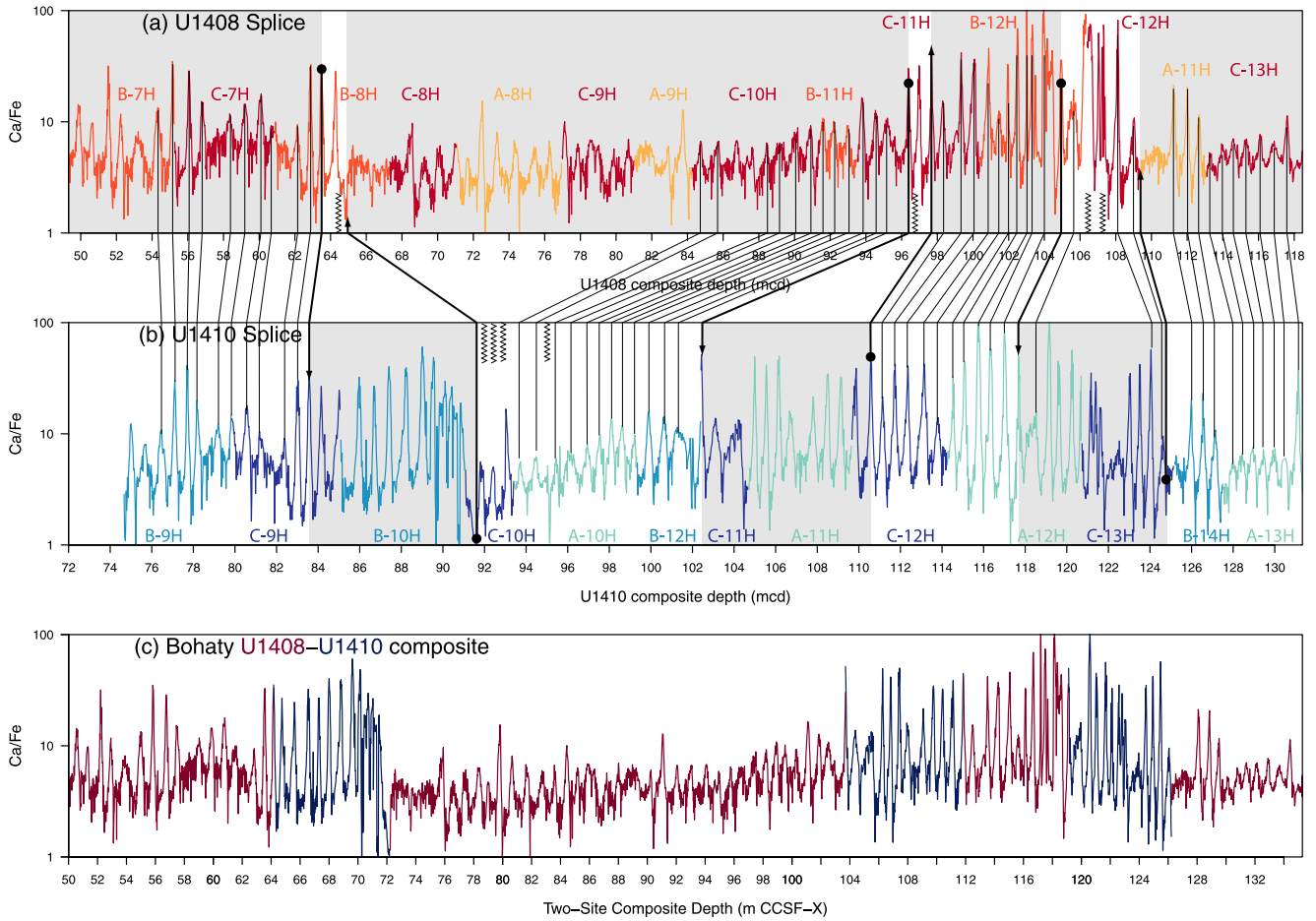

Figure 3. Construction of the upper *Bohaty* composite. The correlation of individual cycles between U1408 and U1410 reveals sections that are present at only one site, and thus represent hiatuses (indicated by zigzagged lines) at the other site. The composite depths scale (m CCSF-X) is constructed from top to bottom by including selected intervals into the composite (following the bold black lines, moving down section).

extremely stable throughout geological history ("astronomical metronome," Hinnov, 2013), with both g_2 and g_5 exhibiting at least one order of magnitude less variability compared to other g-terms (Laskar et al., 2004).

The upper part of the composite (50–160 m CCSF-X) is essentially time-continuous on astronomical time-scales. We make this judgment based on the good fit in terms of bio-, magneto-, and chemostratigraphy (Figures 5 and 6). In the lower part of the composite (160–250 m CCSF-X), magneto- and biostratigraphic datums indicate that more geological time is represented by less stratigraphy compared to the upper part. This could indicate a lower sedimentation rate, but we consider this option unlikely because the lithologic cycles in the lower part are slightly thicker, certainly not thinner, and of the same shape (i.e., the waveform of individual lithological cycles) as in the upper section (Figure 7). Instead, we infer sedimentation rates to be slightly higher in the lower part of the composite, with hiatuses causing more time to be represented by less stratigraphy. We propose four hiatuses throughout the lower part of the composite: at 160.61, 190.21, 214.55, and 221.12 m CCSF-X (Table 2). The upper two hiatuses were placed at abrupt shifts in $\delta^{13}C$ (>0.25‰ over a few centimeters) that coincided with an disturbed amplitude modulation pattern in Ca/Fe. The lower two hiatuses were placed to improve the bio- and chemostratigraphic match between 190.21–214.55 m and 221.12–250 m CCSF-X. For the small section in-between, only limited confidence can be put in the proposed age-depth model, as it is solely based on the chemostratigraphic correlation between the U1408-U1410 composite and the CENOGRID reference curve (i.e., ODP Site 1,263 in this interval).

Together, the two-site composite and its accompanying age-depth model are unequivocal about the astronomical origin of the meter-scale lithological cycles: They are chiefly related to precession (~20 kyr periodicity = ~50

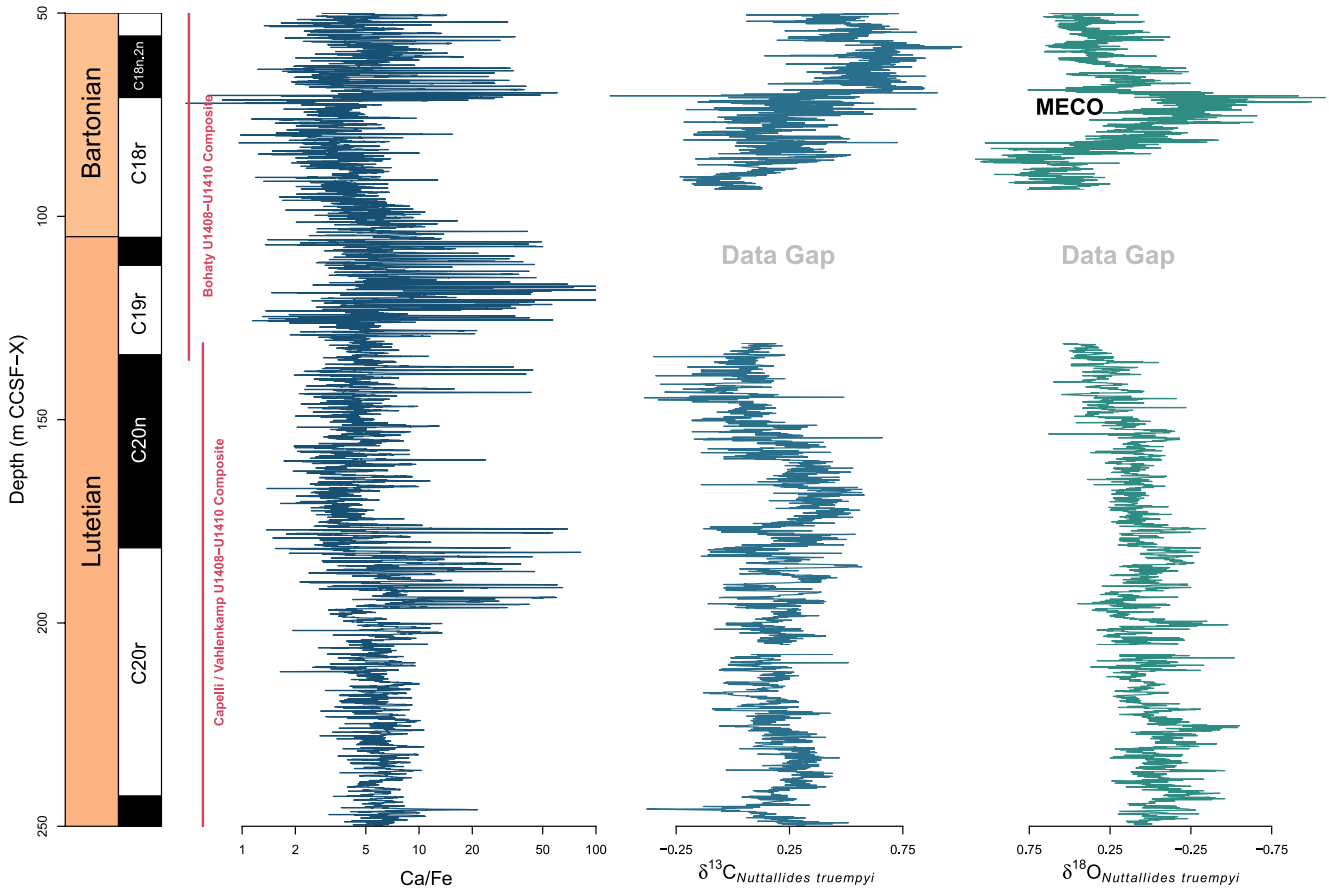

Figure 4. Middle Eocene IODP Sites U1408–U1410 composite section from Newfoundland Ridge (North Atlantic) in the depth-domain. Benthic stable oxygen and carbon isotope series (*Nuttallides truempyi, N* = 3,424) and Ca/Fe series (*N* = 9,662) are plotted along their magnetostratigraphy. The CCSF-X depth scale refers to inter-site mapped depths: This depth-scale arose through meticulous site-to-site correlation, whereby we compiled a stratigraphic sequence as complete as possible through the incorporation of sections present at only one site (i.e., hiatus at the other site) and, where possible, selecting the site with the best coverage in stable isotope data. MECO = Middle Eocene climatic optimum.

cycles/Myr frequency). Indeed, the log(Ca/Fe) multi-taper method spectra display dense clusters of significant frequencies between 40 and 60 cycles/Myr, corresponding to precession (Figures 7e–7h). A smaller cluster also occurs at the obliquity frequency (~25 cycles/Myr), but it is clearly subordinate to the precession cluster. The $\delta^{18}O$ and $\delta^{13}C$ NAFF analyses, on the other hand, show spectral peaks that can be related to obliquity (~25 cycles/Myr), short eccentricity (~10 cycles/Myr) and long eccentricity (~2.5 cycles/Myr) (Figures 8c and 8d). The clear-cut amplitude modulation patterns in Ca/Fe have also been subjected to NAFF analysis and are marked by frequencies that are related to short and long eccentricity, in agreement with astronomical theory (Figure 8b). Based on these elements, we rebut the original obliquity interpretation (Boulila et al., 2018; Boulila & Hinnov, 2022; Vahlenkamp et al., 2018), which was erroneously arrived at for two main underlying reasons. First, the common occurrence of hiatuses in the studied Newfoundland drifts system makes for a complex stratigraphic system. When hiatuses remain undetected, sedimentation rates are underestimated and cycle durations overestimated. Second, Fourier-Transform-based power spectra of Ca/Fe depth-series are dominated by a single peak (or cluster of peaks) that is related to the basic lithological rhythm (Figure 7). Additional peaks at lower frequencies are absent or modestly developed. The latter hampers the application of the classic cyclostratigraphic frequency-ratio method (Sinnesael et al., 2019). There is, of course, the clear bundling of the lithological cycles into groups of 3–5, but this bundling is not sufficiently distinct to discriminate between eccentricity-modulated precession (1:5 ratio) or the amplitude modulation of obliquity by the ~173-kyr s_3–s_6 term (1:4 ratio).

The precession interpretation sheds new light on the mechanistic pathway between astronomical insolation forcing and drift deposition, as well as on sedimentation rates at Sites U1408 and U1410. Readjusted to the precession cycle, the Vahlenkamp et al. (2018) mechanistic model stipulates that enhanced North Atlantic overturning

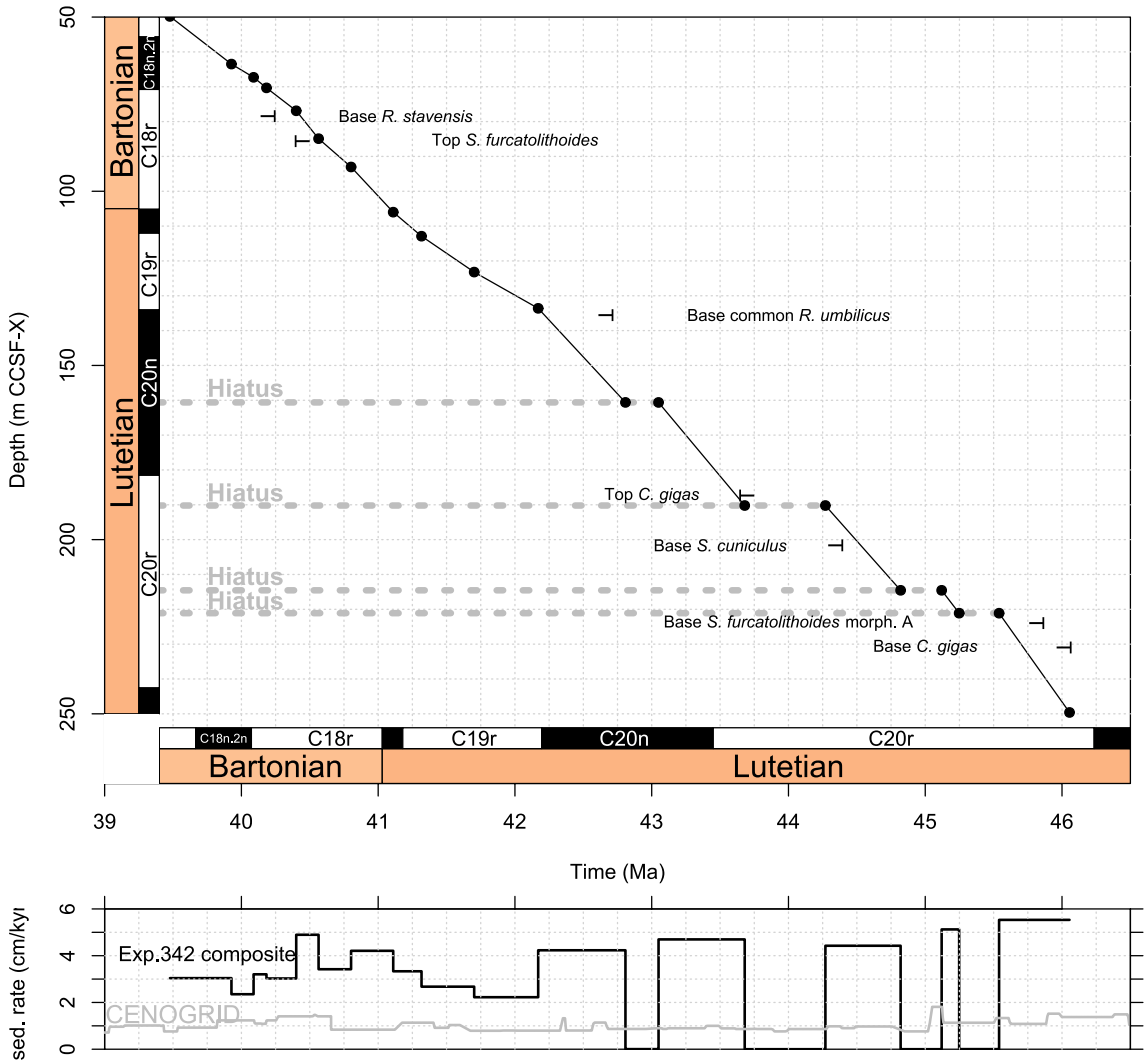

Figure 5. Simple age-depth model for the Middle Eocene composite section from Newfoundland Ridge. Twenty tie-points relate the two-site composite depth scale (m CCSF-X) to geologic age. In-between tie-points linear interpolation is adopted. The age-depth model was constructed by aligning the composite's isotope records with the CENOGRID stratigraphic backbone (Westerhold et al., 2020). Thereby, we considered all available magneto- and biostratigraphic constraints (from both Sites, Table 1), while we explicitly did not assume the sedimentary composite to be time-continuous throughout. The drift Sites U1408–U1410 are characterized by exceptionally high sedimentation rates in comparison with the pelagic reference sites (Walvis Ridge Site 1263 for this part of the Eocene) incorporated into CENOGRID (Westerhold et al., 2020).

is associated with strong cooling of surface waters in the Greenland-Norwegian Sea during precession maxima (when Earth is in the aphelion during northern hemisphere summer). This in turn allows for a vigorous Deep Western Boundary Current, transporting more clay from sources along the northeast Canadian margin to Newfoundland Ridge, leaving behind a low Ca/Fe ratio in the sedimentary record. The precession interpretation also yields sedimentation rate estimates twice as high as previously thought, and thus an exceptionally high time-resolution for the multi-proxy datasets.

5. Constraining the Evolution of the Chaotic Solar System From Geologic Data

5.1. Numerical Analysis of Fundamental Frequencies

To distil astronomical components from the Newfoundland Ridge geologic data, we adopt a strategy that is largely similar to the strategy applied by Olsen et al. (2019). The main difference between Olsen et al. (2019) and this work is that the U1408/U1410 age model was obtained by aligning the benthic isotope records with CENOGRID (Figure 6), whereas Olsen et al. (2019) tuned their time series using a pure 405-kyr g_2–g_5 cosine model.

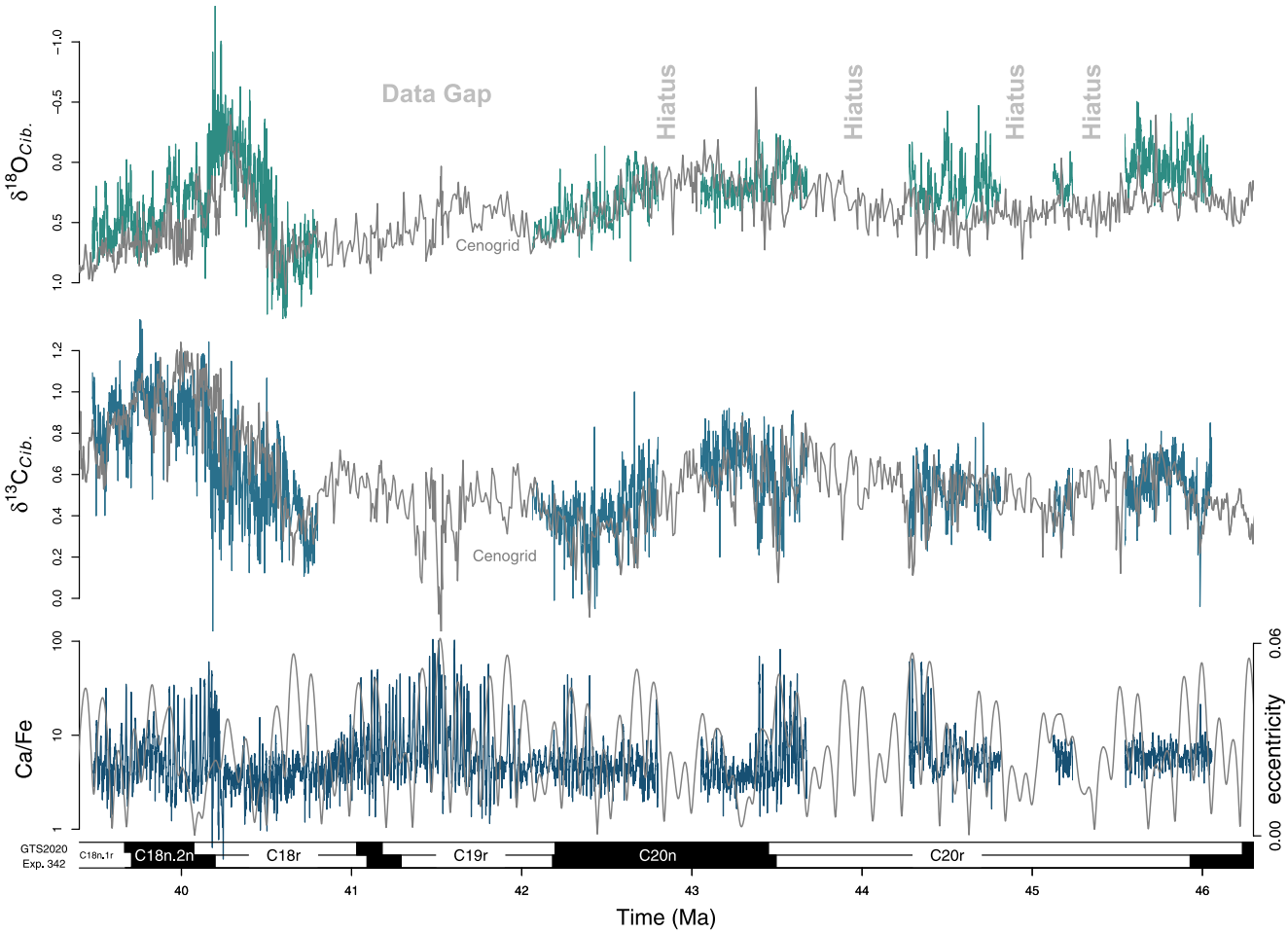

Figure 6. Middle Eocene composite section from Newfoundland Ridge in the time-domain. Site U1408–U1410 isotopic values are shifted toward *Cibicoides (Cib.)* values using the interspecies correction factors of (Katz et al., 2003). The curve in the background of our benthic isotope time-series is the Cenogrid stratigraphic reference (Westerhold et al., 2020). The eccentricity curve in the background of the Ca/Fe time-series is the La11 solution (Laskar et al., 2011b).

The Olsen et al. (2019) tuning completely excludes the inheritance of g-term variability from the astronomical solution, which is not true for our approach. However, the conservative tuning with only 20 tie-points is designed to restrict possible inheritance effects to a minimum (through CENOGRID which is in turn tuned to eccentricity solution La10b). For this study, we deliberately adopt the 20-tie-points age model for NAFF analysis because a tuning of the U1408/U1410 records to a pure 405-kyr cosine model (as in Olsen et al., 2019) led to unsatisfactory age models. The NAFF analysis presented here thus represents a balancing between geochronological accuracy and possible inheritance.

The NAFF method extracts the dominant periodic components from a data series and sorts them by decreasing amplitude. Hence, NAFF provides a tool to objectively detect consistent periodic components in a signal, even when they are buried in noise. An additional convenience of NAFF is that multiple proxies can be used in tandem. This is useful when different astronomical parameters are best registered in different proxies. Here, we apply NAFF to the time-continuous upper part of the middle Eocene composite: between 39.47 and 42.81 Ma for the Ca/Fe time-series, and between 39.47 and 40.82 Ma for the isotopic time-series. The first 70 NAFF components (23 components for the Ca/Fe precession envelope) are shown in Figure 8, but it becomes readily clear that periodic components reminiscent of the periodic components of Earth's orbital eccentricity and spin-axis obliquity and precession occur within the first few high-amplitude components. We employ the NAFF result of the Ca/Fe time-series to select periodic components that correspond to the 5 main precession components ($p + g_{1-5}$). Similarly, the NAFF result of the Ca/Fe precession envelope is used to select periodic components that correspond to various eccentricity components. The long 405-kyr eccentricity component g_2–g_5 constitutes an exception to this

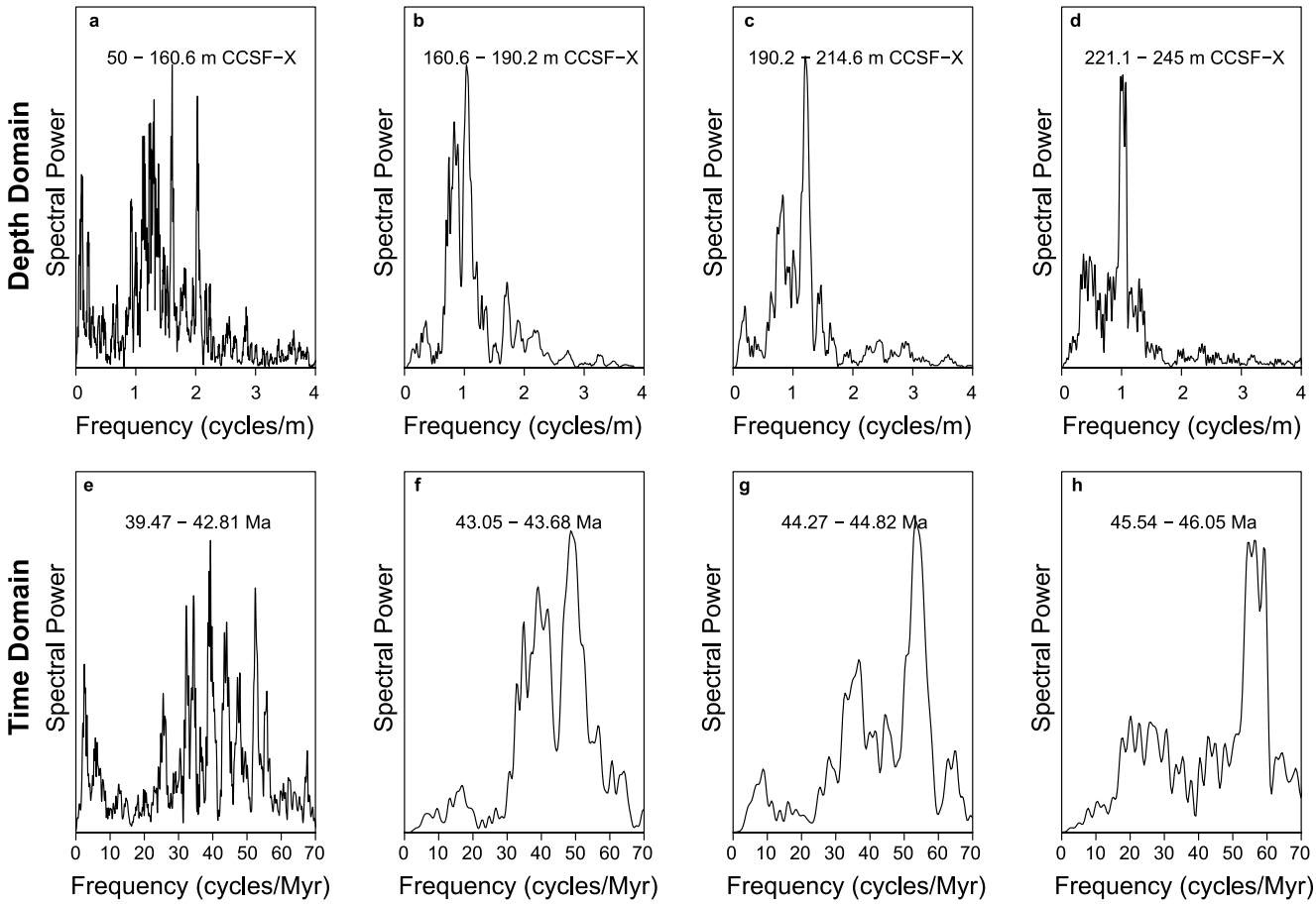

Figure 7. Multi-taper method power spectra of log(Ca/Fe) in the depth and time domain. (a–d) The main lithological cycle depicted by variations in the Ca/Fe ratio reflects rhythmic variations in clay-content. These lithological cycles are slightly thinner (0.65–0.80 m periodicity) in the upper part of the composite (50–160.6 m CCSF-X), compared to the lower part of the composite (∼1 m periodicity). (e–h) In the time domain, the main lithological cycle is ascribed to precession throughout the studied interval.

rule though: While a periodic component associated with g_2–g_5 could be discerned in the NAFF result of the Ca/Fe precession envelope, this component is even more prevalent in the NAFF result of the $\delta^{18}O$ time-series. Moreover, the frequency of the g_2–g_5 component in $\delta^{18}O$ (2.49 cycles/Myr) is closer to the g_2–g_5 frequency predicted by astronomical models (2.46 cycles/Myr), compared to the g_2–g_5 component in the precession amplitude envelope of Ca/Fe (2.85 cycles/Myr). It should be noted that an imprint of g_2–g_5 eccentricity can be discerned in all four NAFF results in Figure 8. Finally, obliquity-related components ($p + s_{2\text{–}4}$ and $p + s_6$) are extracted from the $\delta^{13}C$ NAFF result.

We thus follow a strategy of extracting individual astronomical parameters (precession, obliquity, short eccentricity and 405-kyr eccentricity) from the proxy that most clearly carries its signal. Furthermore, there is also a paleoclimate rationale behind this strategy: precession is the driving force behind local changes in Deep Western Boundary Current velocity, with Ca/Fe as a proxy. Hence, we reconstruct precession by means of Ca/Fe. The impact of precession on insolation and climate, in turn, is amplitude-modulated by eccentricity. Therefore, it is logical to determine the 100-kyr eccentricity component by using the Ca/Fe precession envelope. An obliquity imprint in the U1408/U1410 composite is discernible in the Ca/Fe record, as well as in both isotope records. Here, we work with $\delta^{13}C_{benthic}$ to reconstruct obliquity because it displays the full suite of obliquity frequencies with clear high-amplitude peaks, and because it is not affected by precession-obliquity interference peaks.

Table 3 summarizes all astronomical components that have been identified in the U1408/U1410 Newfoundland Ridge composite series (red bars in Figures 8a–8d). The other frequencies picked up by NAFF analysis (black bars in Figures 8a–8d) reflect the imprint of subordinate astronomical frequencies, interference patterns between different astronomical parameters, and/or climate or sedimentary noise. The NAFF frequencies identified as

Table 2
Stratigraphic Positions and Descriptions of Inferred Hiatuses

Hiatus (m CCSF-X)	Hole	Core	Sec	Offset (cm)	Description
160.61	U1408A	14H	5	7	Cryptic, clay-rich lithology
	U1408C	16H	3	1	Cryptic, clay-rich lithology
	U1410A	15H	4	130	Cryptic. Below cycle 77, different cycle expression between the two sites hampers correlation (Figure 2)
190.21	U1408A	17H	2	112	Sharp contact: likely erosional surface within clay-rich lithology
	U1408C	19H	2	94	Sharp contact: likely erosional surface within clay-rich lithology
	U1410A	17X	5	33	Cryptic, clay-rich lithology
214.55	U1408B	21X	2	148	Cryptic, but disturbed interval ~80 cm higher up in the section within clay-rich lithology.
	U1408A	19H	4	126	Cryptic, but dark horizontal bands ~60 cm higher up in the section
	U1410A	19X	4	140	Cryptic, but dark horizontal bands within clay-rich lithology.
221.12	U1408A	20H	1	149	Cryptic
	U1410A	20X	1	93	Disturbed interval
	U1410C	20X	2	42	Cryptic

astronomical components (red bars) allow the reconstruction of fundamental astronomical frequencies at ~41 Ma (i.e., the mid-point of the analyzed interval), just by assuming that the outer Solar System is stable over the age of the Earth. Concretely, we assume the g_5 and s_6 frequencies to be invariant through geologic time, and adopt their present-day values as reported in Laskar et al. (2004). These fundamental frequencies are related to Jupiter and Saturn, respectively, and their assumed stability is due to the large mass of these planets (317.8 and 95.2 times the mass of the Earth). With these assumptions, we first calculate g_2 from the δ^{18}O-extracted g_2–g_5 periodic component. Subsequently, we calculate g_1 from g_2–g_1. After these two steps, we obtain an overdetermined system and can directly calculate g_3 from g_3–g_5 as well as from g_3–g_2. The same goes for g_4, which is calculated from g_4–g_5, g_4–g_2, and (g_4–g_2)−(g_2–g_5). The resulting g_i frequencies are compared to the La04 astronomical model, as well as to an independent reconstruction from Walvis Ridge early Eocene data by Meyers and Malinverno (2018). Our results for g_4 are consistent with La04, but our estimates for the g_1 and g_3 frequencies are up to 4% lower than the minimum value predicted by the La04 model, and our g_2 frequency estimate is ~0.5% higher. Interestingly, Meyers and Malinverno (2018) observed an analogous data-model mismatch. These authors explain the mismatch by pointing out that Laskar et al. (2004) adopts 20-Myr averaging intervals before plotting the variation in secular frequencies $g_{1–4}$, whereas the geology-based reconstructions for the Eocene span much shorter time intervals.

The NAFF result for g_3 is remarkable because a 4% lower g_3 (~16.705"/year) in combination with a roughly constant g_4 (~17.769"/year) would imply a g_4–g_3 eccentricity term of ~1.064"/year. This frequency is equivalent to a g_4–g_3 eccentricity term with a periodicity of 1.22 Myr. In the present day, the g_4–g_3 term is an eccentricity cycle with a periodicity around 2.4 Myr (~0.544″/year). Together with the 1.2-Myr-long s_4–s_3 obliquity modulation cycle, the g_4–g_3 eccentricity term is one of the "Grand Cycles" in cyclostratigraphy (Hinnov, 2013). However, this 2:1 ratio between g_4–g_3 and s_4–s_3 may not have been steadfast through geologic time. Astronomical models predict that the g_4–g_3 term can quickly transition from its "normal" frequency ~0.544″/year to a value >0.9″/year, creating a new 1:1 resonance between the two "Grand Cycles" (Hoang et al., 2021). In other words, the

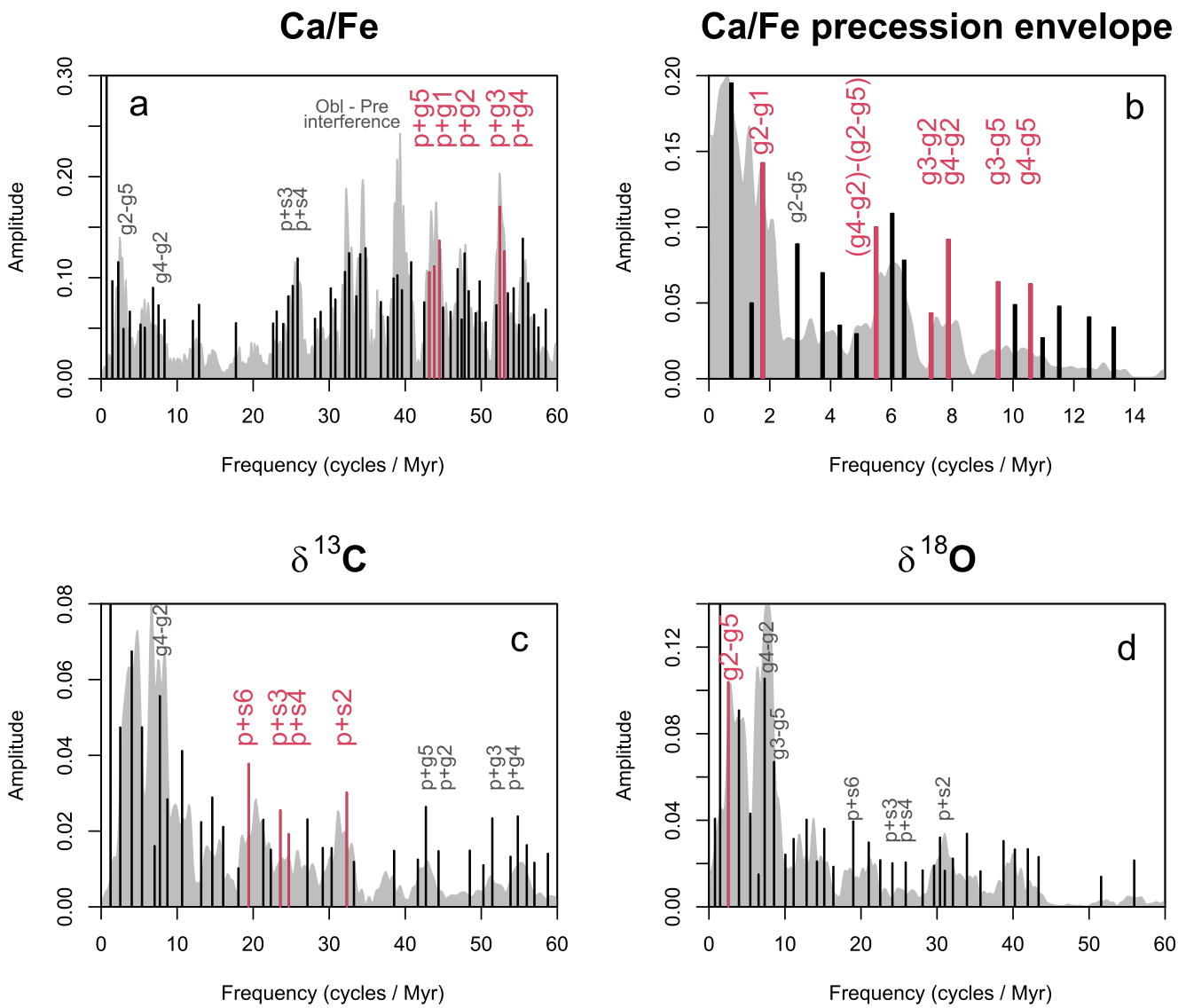

Figure 8. Extraction of fundamental astronomical frequencies with NAFF. Precession ($p + g_i$), obliquity ($p + s_i$) and eccentricity (g_i-g_j) arguments are differently expressed in the different proxies. We use log(Ca/Fe) to extract precession, $\delta^{13}C$ for obliquity, the precession envelope of Ca/Fe for short eccentricity and $\delta^{18}O$ for long eccentricity. Selected NAFF frequencies (bar chart) are indicated in red and labeled with their associated astronomical argument (listed in Table 3). Multi-taper method spectra are shown in the background.

g_4–g_3 periodicity has the potential to temporarily change from a ~2.4 Myr period (libration) to a ~1.2 Myr period (circulation). While theoretic astronomical models do predict that such g_4–g_3 transitions occurred in the geologic past, they consider it unlikely that this would have occurred in the last 50 million years (Hoang et al., 2021). That being said, the exact timing of such chaotic transitions remains an open question. This is because, on the one hand, astronomical models are strongly dependent on initial conditions, and on the other hand, it is difficult to extract these chaotic transitions from the geologic record. To date, there are only two publications that report on tentative geologic indications of chaotic transitions around 52 Ma (Westerhold et al., 2017) and 87 Ma (Ma et al., 2017). In case our reconstructed values for g_3 and g_4 are accurate, we provide a third possible timing for a chaotic resonance transition in Earth's history, around the Middle Eocene Climatic Optimum. In this study, the robustness of this interpretation is further scrutinized with TimeOptMCMC (see Section 5.2).

The middle Eocene precession constant is estimated in nine different ways, using five different precession arguments ($p + g_{1-5}$), one obliquity argument ($p + s_6$), and multiple estimates for g_3 and g_4 (Table 3). The nine estimates range between 50.088″/year and 51.62″/year, with a median value of 51.20″/year and an interquartile range between 50.88

Table 3
Reconstruction of Astronomical Components

Argument	Frequency (cycles/Myr)	Frequency (″/year)	Period (kyr)	Proxy
$g2–g5$	2.495	3.233	400.9	$\delta^{18}O$
$g3–g2$	7.254	9.401	137.9	Ca/Fe envelope
$g4–g2$	7.826	10.143	127.8	Ca/Fe envelope
$g3–g5$	9.461	12.261	105.7	Ca/Fe envelope
$g4–g5$	10.522	13.637	95.0	Ca/Fe envelope
$(g4–g2)–(g2–g5)$	5.445	7.057	183.7	Ca/Fe envelope
$g2–g1$	1.717	2.226	582.3	Ca/Fe envelope
$p + s6$	19.345	25.071	51.7	$\delta^{13}C$
$p + s3$	23.522	30.485	42.5	$\delta^{13}C$
$p + s4$	24.614	31.900	40.6	$\delta^{13}C$
$p + s2$	32.264	41.814	31.0	$\delta^{13}C$
$p + g5$	43.120	55.884	23.2	Ca/Fe
$p + g1$	43.746	56.695	22.9	Ca/Fe
$p + g2$	44.428	57.579	22.5	Ca/Fe
$p + g3$	52.389	67.896	19.1	Ca/Fe
$p + g4$	52.982	68.665	18.9	Ca/Fe

Secular fundamental frequency	Frequency (″/year)	Argument used for calculation
$g5$	4.2575	Assumed constant
$g2$	7.4905	$g5–g2$
$g1$	5.2649	$g2–g1$
$g3$	16.5186	$g3–g5$
$g3$	16.8914	$g3–g2$
$g4$	17.8945	$g4–g5$
$g4$	17.6336	$g4–g2$
$g4$	17.7803	$(g4–g2)–(g2–g5)$
$s3$	−26.3478	Assumed constant

Precession constant	Frequency (″/year)	Argument used for calculation	Secular frequency used for calculation
p	51.6262	$p + g5$	$g5 = 4.2575$
p	50.0888	$p + g2$	$g2 = 7.4905$
p	51.4300	$p + g1$	$g1 = 5.2649$
p	51.3771	$p + g3$	$g3 = 16.5186$
p	51.0043	$p + g3$	$g3 = 16.8914$
p	50.7703	$p + g4$	$g4 = 17.8945$
p	51.0312	$p + g4$	$g4 = 17.6336$
p	50.8845	$p + g4$	$g4 = 17.7803$
p	51.4191	$p + s6$	$s6 = −26.3478$

Note. We reconstruct Secular g-terms and the precession constant based on the identification of astronomical arguments in the U1408–U1410 middle Eocene composite.

and 51.42″/year (boxplot in Figure 9e). The spread between the nine precession constant p estimates gives a sense of the uncertainty related to its reconstruction, yet it does not constitute a full-blown error propagation analysis. Uncertainties arise from several assumptions that went into age-depth modeling, while associating NAFF frequencies to astronomical parameters also requires user decisions. These uncertainties are hardly quantifiable and the propagation of uncertainties into NAFF results is not attempted in the framework of this work. Instead, the TimeOptMCMC

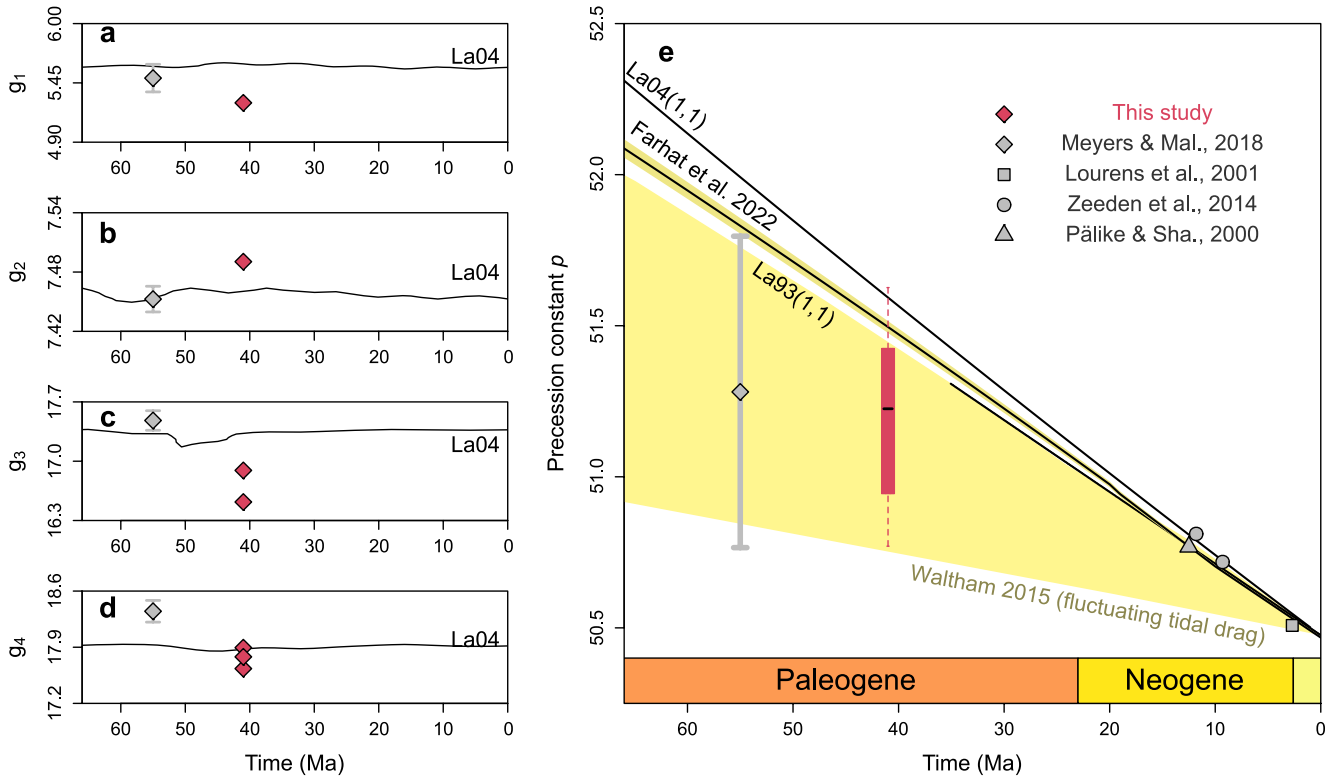

Figure 9. Reconstruction of astronomical components by NAFF analysis. (a–d) Middle Eocene reconstructed g-terms (red diamonds), compared to an Early Eocene reconstruction by Meyers and Malinverno (2018) (gray diamond), and compared the corresponding term in the La04 solution. (e) Middle Eocene reconstructed precession constant (red boxplot), compared to other Cenozoic reconstructions (gray symbols) and compared to different astronomical models (black lines and gray shaded area).

technique is adopted in §5.2. This algorithm extracts the g-terms and precession constant p from the U1408/U1410 composite, while simultaneously estimating their uncertainties with a Bayesian Monte Carlo approach.

5.2. TimeOptMCMC

The NAFF technique has the advantage of being intuitive. It also allows working with multiple proxies when different astronomical parameters are best recorded by a range of different proxies. Major drawbacks for the NAFF technique reside in the fact that it is difficult to quantify uncertainties and the selection of astronomical frequencies depends on expert judgment. To circumvent both disadvantages and to scrutinize the NAFF results, we apply TimeOptMCMC on the time-continuous log(Ca/Fe) time-series between 39.47 and 42.81 Ma (allowing for time-axis perturbations of ±10%). The precession-dominated log(Ca/Fe) time-series and its strong amplitude modulation are well-suited for the TimeOptMCMC approach because this method is simultaneously evaluating the concentration of spectral power at the expected astronomical frequencies, and the amplitude modulation of precession by eccentricity. First, we utilized prior distributions (gray distributions in Figure 10) that have identical mean values compared to the Eocene Walvis Ridge analysis in Meyers and Malinverno (2018). The standard deviations of the prior distributions of the g-terms are however twice as large as in Meyers and Malinverno (2018). This choice was made to give TimeOptMCMC the freedom to test astronomical configurations that deviate further from the nominal astronomical solution, like for example, the 4% lower g_3 frequencies suggested by NAFF.

The posterior distribution for g_1 is bimodal, with the lower mode being in agreement with the NAFF result (Figure 10a). The g_2 posterior distribution is similar to the prior distribution. The NAFF g_2 estimate occurs within the high probability range of the Bayesian approach (Figure 10b). The similarity between g_2 prior and posterior distributions is an important observation, as it underlines the stability and invariability of the g_5–g_2 405-kyr eccentricity component. Indeed, our results once again affirm the status of the 405-kyr eccentricity term as the prime astronomical metronome for geologic time-keeping. The g_3 posterior distribution is multimodal with the first mode occurring close to the predicted g_3 frequency in the La04 astronomical solution (Figure 10c). The second mode, however, is in

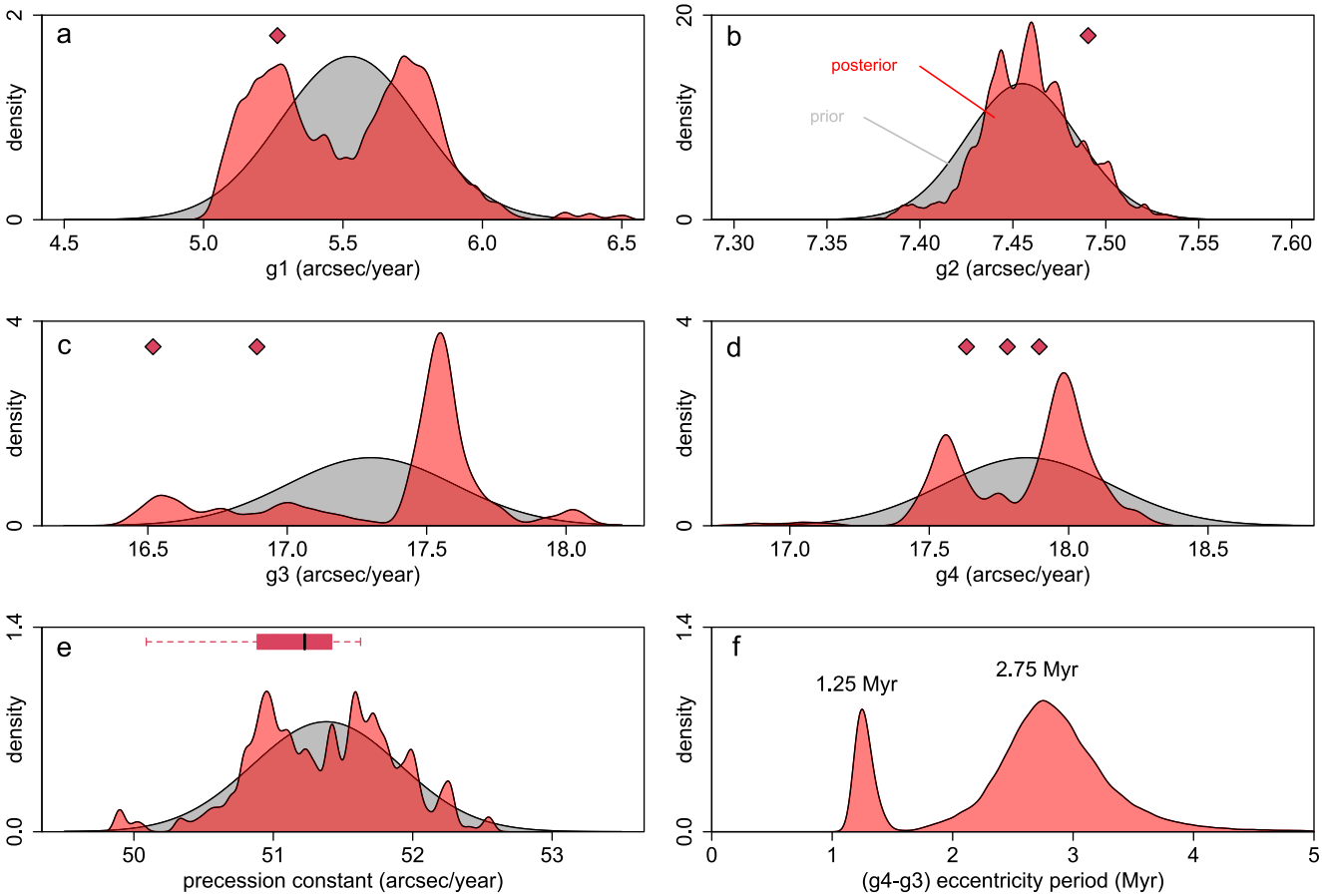

Figure 10. Summary of TimeOptMCMC prior and posterior distributions for the 39.5–43 Ma Newfoundland Ridge two-site composite log(Ca/Fe) data. (a–e) Prior (gray distribution) and posterior (red distribution) for the different g-terms and precession constant are compared to the results of the NAFF approach (red diamonds, see also Table 3). (f) The distribution of the very-long (g_4–g_3) eccentricity period in the TimeOptMCMC simulations shows a bimodal distribution with one population indicating libration (~2.75 Myr) and another population indicating circulation (~1.2 Myr).

good agreement with the 4%-lower g_3 result obtained through NAFF analysis. We note that this second mode is at the lowermost end of the prior distribution, which implies that such low g_3 frequencies are relatively underexplored by the TimeOptMCMC algorithm. Nevertheless, the second g_3 mode illustrates that, when the algorithm examines relatively low g_3 frequencies, high likelihoods are obtained. The g_4 posterior distribution is significantly narrower than the prior distribution with two modes close to the predicted value in the La04 solution (Figure 10d). We came to a similar observation based on the g_4 NAFF results and we thus consider the g_4 results of both techniques to be well-aligned. The same goes for the NAFF and TimeOptMCMC results for the precession parameter p (Figure 10e).

By plotting the posterior distribution of the g_4–g_3 term in the TimeOptMCMC analyses (Figure 10f), we examined a possible chaotic resonance transition around 41 Ma as it was suggested by NAFF analysis. The g_4–g_3 term in the TimeOptMCMC simulations is bimodally distributed, with a first mode around 2.75 Myr periodicities and a narrow but dense mode around 1.25 Myr. The TimeOptMCMC simulations thus provide support for a possible chaotic resonance transition between libration (~2.4 Myr g_4–g_3 period) and circulation (~1.2 Myr g_4–g_3 period) around 41 Ma.

The NAFF and TimeOptMCMC results are broadly compatible in the sense that they both hint at the possibility for a relatively low g_3 frequency around 41 Ma. To explore this possibility further, we updated our prior beliefs on the g-term frequencies with new information observed through NAFF analysis (Table 3). We reran TimeOptMCMC, now shifting the average values for the g_1 to g_4 fundamental frequencies to 5.2649, 7.4905, 16.705, and 17.769″/year, respectively. These values represent the mean values of the updated prior distributions, depicted in gray on Figure 11. The resulting posterior g-term and precession constant p posterior distributions are shown as red distributions in Figure 11, and amount to 5.2956 ± 0.2485”/year for g_1, 7.4828 ± 0.0289”/year for g_2, 16.6421 ± 0.2786”/year for g_3, 17.6000 ± 0.2608”/year for g_4 and 51.2805 ± 0.5564”/year for the precession constant (uncertainties reflect ±1σ). We consider these values to be the best estimate of these frequencies from the between 39.5 and

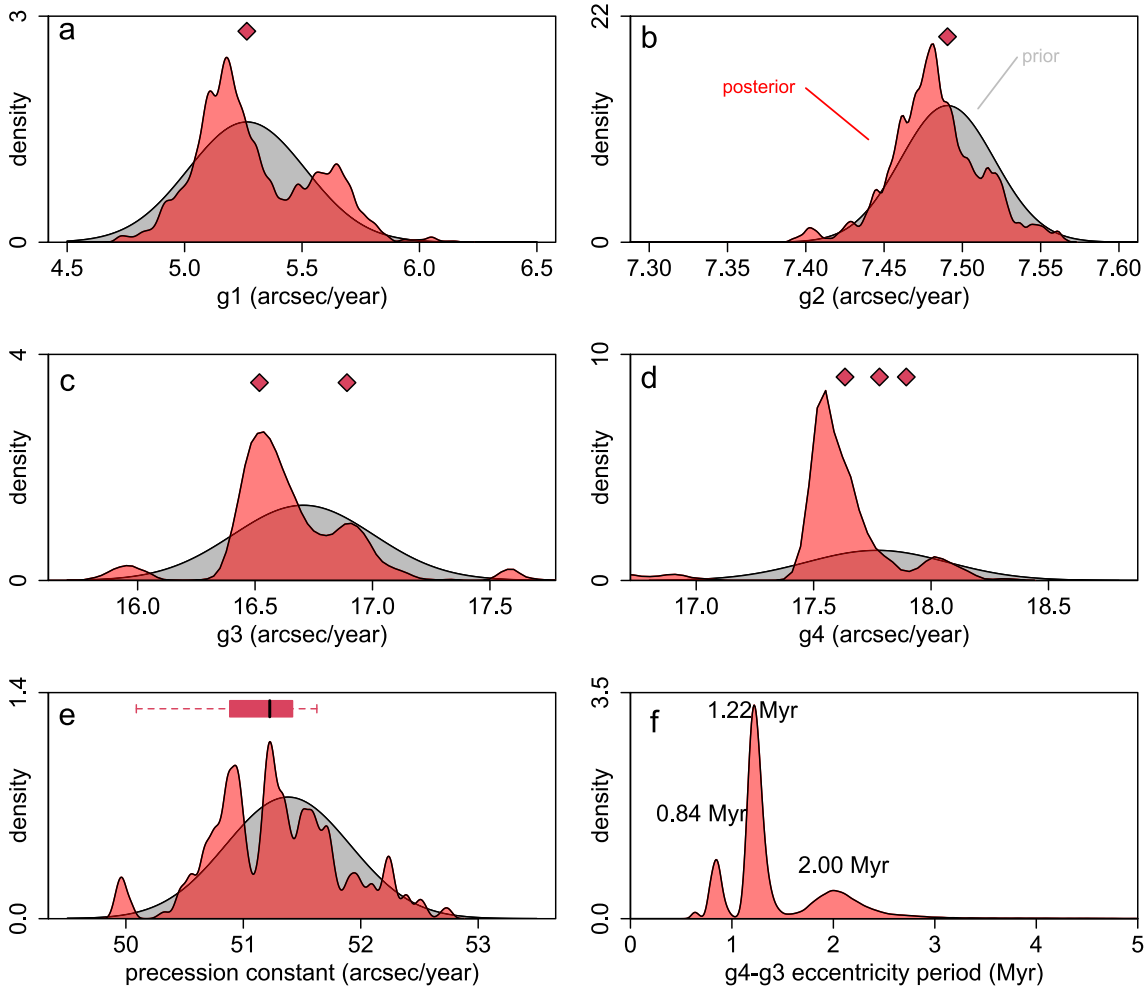

Figure 11. Summary of TimeOptMCMC results, ran with the updated prior belief that the g_3 frequency was ~4% lower around 41 Ma. (a–e) Prior (gray distribution) and posterior (red distribution) for the different g-terms and precession constant are compared to the results of the NAFF approach (red diamonds, see also Table 3). (f) The distribution of the very-long (g_4–g_3) eccentricity period in the TimeOptMCMC simulations shows a bimodal distribution with the main mode indicating circulation (~1.2 Myr).

42.8 Ma dataset studied, and thus serve as a possible target for subsequent generations of astronomical solution at that time (Table 4, Figure 12). Moreover, the posterior g-term and precession distributions (Figure 11) have single or multiple modes that are in excellent agreement with the NAFF reconstructions (Figures 9 and 12). We note that such agreement is to be expected as both methods were applied to the same proxy time-series. Yet, this is the first time the two techniques are compared, and confirmed to be compatible despite their major methodological differences. Thus, our conclusion that the evolution of the fundamental frequencies through geologic time exhibited much greater Myr-scale variability than previously assumed is corroborated by both NAFF and TimeOptMCMC results.

Table 4
Targets for Astronomical Solutions Between 39.5 and 42.8 Ma, as Extracted From the U1408–U1410 Composite by Using TimeOptMCMC With Updated Prior Beliefs (as in Figures 11 and 12)

Secular fundamental frequency	Frequency (“/year ± 1σ)
g_1	5.2956 ± 0.2485
g_2	7.4828 ± 0.0289
g_3	16.6421 ± 0.2786
g_4	17.6000 ± 0.2608
Precession constant p	51.2805 ± 0.5564

5.3. Implications for Earth-Moon Dynamics

Our precession constant estimates are markedly lower compared to the corresponding value in the La04(1,1) astronomical solution (Figure 12e). Yet, it is in excellent agreement with the Waltham (2015) calculations that include time-fluctuating tidal friction. The early Eocene precession constant reconstruction based on Walvis Ridge data (Meyers & Malinverno, 2018) provides additional support for the Waltham tidal friction model: Both their and our Eocene reconstructions suggest that tidal friction is overestimated

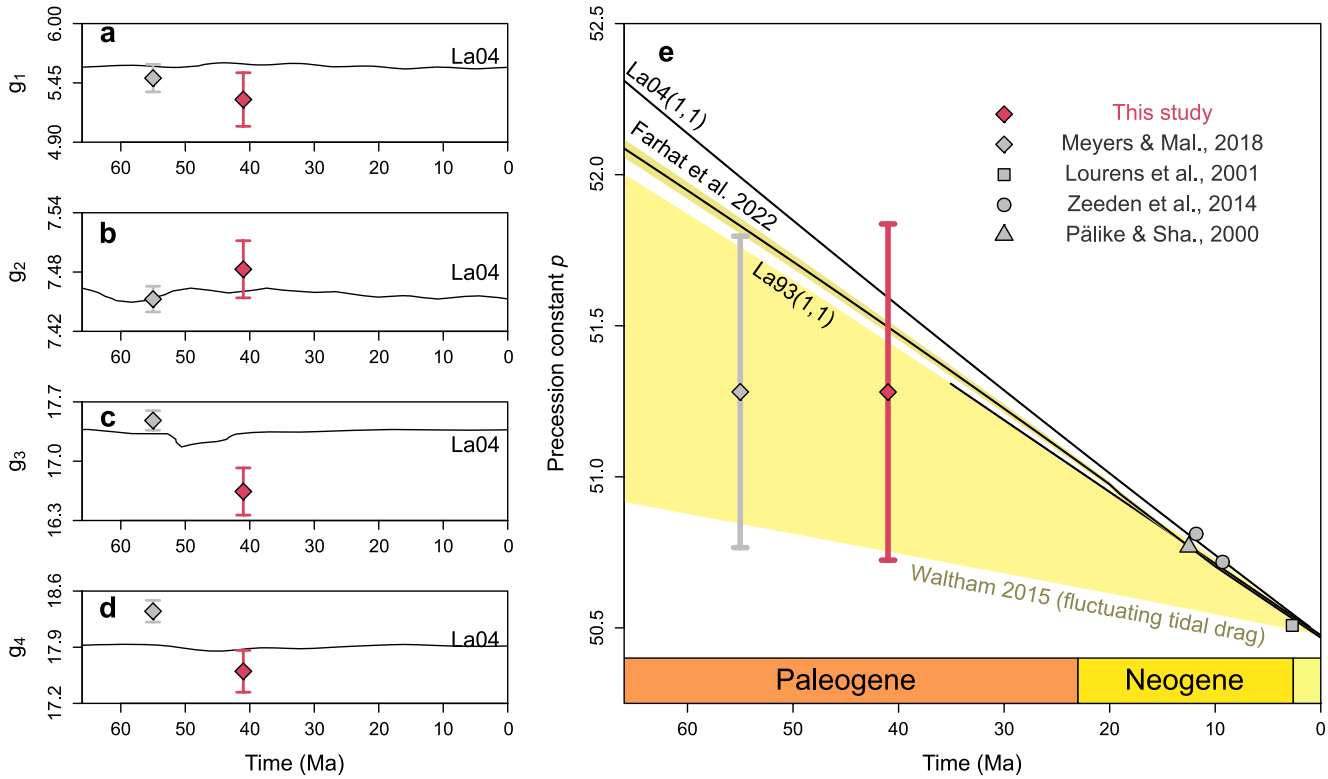

Figure 12. Reconstruction of astronomical components by TimeOptMCMC analysis. (a–d) Middle Eocene reconstructed g-terms (red diamond), compared to an Early Eocene reconstruction by Meyers and Malinverno (2018) (gray diamond), and compared the corresponding term in the La04 solution. (e) Middle Eocene reconstructed precession constant (red), compared to other Cenozoic reconstructions (gray symbols) and compared to different astronomical models (black lines and gray-shaded area).

in the nominal La93(1,1) and La04(1,1) solutions (Laskar, Joutel, et al., 1993; Lasker, Robutel, et al., 2004), at least when going back into the Paleogene. When only these two Eocene data points are considered, we find a much better model-data fit when considering an astronomical solutions with a tidal dissipation that is considerably lower (~20% lower) compared to the present-day value (as used in La93(1,1); see Materials and Methods; Figures 9e and 12e). However, geology-based reconstructions of tidal dissipation and dynamic ellipticity for the Neogene (Lourens et al., 2001; Pälike & Shackleton, 2000; Zeeden et al., 2014) demonstrate good agreement with the evolution of the precession constant as implemented in the nominal Laskar solutions and the Farhat et al. (2022) model (Figure 12e). Therefore, we infer that the tidal dissipation of rotational energy must have occurred at a relatively low pace throughout the Paleogene, in agreement with numerical tidal models (e.g., Green et al., 2017), after which a marked increase in tidal drag caused a much more rapid decrease of the precession constant during the Neogene and Quaternary.

The methodology we present here is unique in that it starts from a conservative age-depth model that was constructed prior to, and independent of, the extraction of astronomical components. While we find larger-than-expected variability in astronomical g-terms, our tidal dissipation reconstructions support similar results reported by previous studies (Meyers & Malinverno, 2018; Zeebe & Lourens, 2022). Therewith, our results urge Paleogene workers to move on from the default (1,1) setting for dynamical ellipticity and tidal dissipation in astronomical solutions when assessing detailed obliquity-precession interference patterns.

6. Conclusion

The extraction of astronomical components presented here exploits the particularly cyclic middle Eocene drift deposits on Newfoundland Ridge, cored during IODP Expedition 342. The lithologic clay-content cycles are now firmly identified as the imprint of climatic precession. This interpretation was made based on a carefully constructed two-site composite, in combination with an age-depth model that solely consists of only 20 age-depth tie-points. This feature of our analysis allows the classic cyclostratigraphic approach to be reversed while

minimizing the risk for circular reasoning: Different rhythmic components in high-resolution proxy-series served the reconstruction of four g-terms and the precession constant p. These reconstructions provide novel constraints on the Cenozoic evolution of our solar system. First, the variability in g-term frequencies on million-year timescales has previously been underestimated. Second, the internally consistent evidence for a relatively slow tidal energy dissipation throughout the Paleogene and a strong increase during the Neogene caps a long-standing debate. Both pieces of information (g-terms and p, Table 4 and Figure 12) constitute targets that astronomers can use to extend the reliability of astronomical insolation models in geologic time.

Data Availability Statement

X-Ray Fluoresence and benthic isotope proxy data is available through PANGAEA (De Vleeschouwer, 2022). The online Graphical User Interface (GUI) to quantify the effect of dynamical ellipticity and tidal dissipation on precession constant p using the La1993 formulation is available through https://paloz.marum.de/AstroComputation/index.html (Pälike, 2021a). The NAFF software is available through https://paloz.marum.de/confluence/display/ESPUBLIC/NAFF (Pälike, 2021b). The R scripts used to generate Figures 4–12 are available through Zenodo (De Vleeschouwer, 2023).

Acknowledgments
This research used samples and data provided by the International Ocean Discovery Program (IODP) and its predecessors, a program sponsored by NSF and participating countries under the management of Joint Oceanographic Institutions. XRF core-scanning was made possible thanks to the instrumentation and support of the SIO Geological Collections at the Scripps Institution of Oceanography, University of California San Diego (managed by A. Hangsterfer). We warmly thank all shipboard and on-shore scientists that contributed to XRF core scanning in Bremen and San Diego. Financial support was provided by the National Science Foundation (NSF) to PMH (NSF Award #1335261) and JCZ (NSF Award #1334209) and the Belgian American Educational Foundation (B.A.E.F.) and the Fulbright Commission of Belgium and Luxemburg to SD. B. Erkkila, M. Wint, L. Elder and numerous students of the Yale Analytical and Stable Isotope Center, D. Andreasen of the UCSC Stable Isotope Laboratory, Megan Wilding and Bastian Hambach of the NOCS stable isotope lab, and Henning Kuhnert and the team of the MARUM isotope lab are thanked for assistance with isotopic analyses. All Bayesian Morkov Chain Monte Carlo analyses were run on the PALMA-II High Performance Computing cluster provided by the University of Münster. Open Access funding enabled and organized by Projekt DEAL.

References

Berger, A., Loutre, M. F., & Laskar, J. (1992). Stability of the astronomical frequencies over the Earth's history for paleoclimate studies. *Science*, *255*(5044), 560–566. https://doi.org/10.1126/science.255.5044.560

Bohaty, S. M., & Zachos, J. C. (2003). Significant Southern ocean warming event in the late middle Eocene. *Geology*, *31*(11), 1017–1020. https://doi.org/10.1130/G19800.1

Bohaty, S. M., Zachos, J. C., Florindo, F., & Delaney, M. L. (2009). Coupled greenhouse warming and deep-sea acidification in the Middle Eocene. *Paleoceanography*, *24*(2). https://doi.org/10.1029/2008PA001676

Boulila, S., & Hinnov, L. A. (2022). Constraints on Earth-Moon dynamical parameters from Eocene cyclostratigraphy. *Global and Planetary Change*, *216*, 103925. https://doi.org/10.1016/j.gloplacha.2022.103925

Boulila, S., Vahlenkamp, M., De Vleeschouwer, D., Laskar, J., Yamamoto, Y., Palike, H., et al. (2018). Towards a robust and consistent Middle Eocene astronomical timescale. *Earth and Planetary Science Letters*, *486*, 94–107. https://doi.org/10.1016/j.epsl.2018.01.003

Bown, P. R., & Newsam, C. (2017). Calcareous nannofossils from the Eocene North Atlantic ocean (IODP expedition 342 sites U1403-1411). *Journal of Nannoplankton Research*, *37*(1), 25–60.

Boyle, P. R., Romans, B. W., Tucholke, B. E., Norris, R. D., Swift, S. A., & Sexton, P. F. (2017). Cenozoic North Atlantic deep circulation history recorded in contourite drifts, offshore Newfoundland, Canada. *Marine Geology*, *385*, 185–203. https://doi.org/10.1016/j.margeo.2016.12.014

Cappelli, C., Bown, P. R., De Riu, M., & Agnini, C. (2020). Middle Eocene large coccolithaceans: Biostratigraphic implications and paleoclimatic clues. *Marine Micropaleontology*, *154*, 101812. https://doi.org/10.1016/j.marmicro.2019.101812

Cappelli, C., Bown, P. R., de Riu, M., & Agnini, C. (2021). The evolution of Eocene (Ypresian/Lutetian) sphenoliths: Biostratigraphic implications and paleoceanographic significance from North Atlantic site IODP U1410. *Newsletters on Stratigraphy*, *54*(4), 405–431. https://doi.org/10.1127/nos/2020/0606

Cappelli, C., Bown, P. R., Westerhold, T., Bohaty, S. M., Riu, M., Lobba, V., et al. (2019). The early to Middle Eocene transition: An integrated calcareous nannofossil and stable isotope record from the Northwest Atlantic Ocean (Integrated Ocean Drilling Program site U1410). *Paleoceanography and Paleoclimatology*, *34*(12), 1913–1930. https://doi.org/10.1029/2019pa003686

Cramwinckel, M. J., Coxall, H. K., Sliwinska, K. K., Polling, M., Harper, D. T., Bijl, P. K., et al. (2020). A warm, stratified, and restricted Labrador Sea across the Middle Eocene and its climatic optimum. *Paleoceanography and Paleoclimatology*, *35*(10), e2020PA003932. https://doi.org/10.1029/2020PA003932

Daher, H., Arbic, B. K., Williams, J. G., Ansong, J. K., Boggs, D. H., Muller, M., et al. (2021). Long-Term Earth-Moon evolution with high-level orbit and ocean tide models. *Journal of Geophysical Research: Planets*, *126*(12), e2021JE006875. https://doi.org/10.1029/2021JE006875

De Vleeschouwer, D. (2022). Benthic stable isotopes and XRF element counts of IODP Sites 342-U1408 and 342-U1410 [Dataset]. PANGAEA. https://doi.org/10.1594/PANGAEA.943968

De Vleeschouwer, D. (2023). North Atlantic Drift Sediments Constrain Eocene Tidal Dissipation and the Evolution of the Earth-Moon System: Figures [Software][Dataset]. Zenodo. https://doi.org/10.5281/zenodo.7517487

Dinarès-Turell, J., Martinez-Braceras, N., & Payros, A. (2018). High-resolution integrated cyclostratigraphy from the Oyambre section (Cantabria, N Iberian Peninsula): Constraints for orbital tuning and correlation of middle Eocene Atlantic deep-sea records. *Geochemistry, Geophysics, Geosystems*, *19*(3), 787–806. https://doi.org/10.1002/2017GC007367

Farhat, M., Auclair-Desrotour, P., Boue, G., & Laskar, J. (2022). The resonant tidal evolution of the Earth-Moon distance. *Astronomy & Astrophysics*, *665*, 1–20. https://doi.org/10.1051/0004-6361/202243445

Green, J. A. M., Huber, M., Waltham, D., Buzan, J., & Wells, M. (2017). Explicitly modelled deep-time tidal dissipation and its implication for Lunar history. *Earth and Planetary Science Letters*, *461*, 46–53. https://doi.org/10.1016/j.epsl.2016.12.038

Hansen, K. S. (1982). Secular effects of oceanic tidal dissipation on the Moon's orbit and the Earth's rotation. *Reviews of Geophysics*, *20*(3), 457–480. https://doi.org/10.1029/RG020i003p00457

Hinnov, L. A. (2013). Cyclostratigraphy and its revolutionizing applications in the Earth and planetary sciences. *The Geological Society of America Bulletin*, *125*(11–12), 1703–1734. https://doi.org/10.1130/b30934.1

Hoang, N. H., Mogavero, F., & Laskar, J. (2021). Chaotic diffusion of the fundamental frequencies in the Solar System. *A&A*, *654*, A156. https://doi.org/10.1051/0004-6361/202140989

Katz, M. E., Katz, D. R., Wright, J. D., Miller, K. G., Pak, D. K., Shackleton, N. J., & Thomas, E. (2003). Early Cenozoic benthic foraminiferal isotopes: Species reliability and interspecies correction factors. *Paleoceanography*, *18*(2). https://doi.org/10.1029/2002pa000798

Kent, D. V., Olsen, P. E., Rasmussen, C., Lepre, C., Mundil, R., Irmis, R. B., et al. (2018). Empirical evidence for stability of the 405-kiloyear Jupiter–Venus eccentricity cycle over hundreds of millions of years. *Proceedings of the National Academy of Sciences*, *115*(24), 6153–6158. https://doi.org/10.1073/pnas.1800891115

Laskar, J. (1990). The chaotic motion of the solar system: A numerical estimate of the size of the chaotic zones. *Icarus*, *88*(2), 266–291. https://doi.org/10.1016/0019-1035(90)90084-M

Laskar, J. (1999). The limits of Earth orbital calculations for geological time-scale use. *Philosophical Transactions of the Royal Society of London A: Mathematical, Physical and Engineering Sciences*, *357*(1757), 1735–1759. https://doi.org/10.1098/rsta.1999.0399

Laskar, J., Fienga, A., Gastineau, M., & Manche, H. (2011a). La2010: A new orbital solution for the long-term motion of the Earth. *Astronomy & Astrophysics*, *532*, A89. https://doi.org/10.1051/0004-6361/201116836

Laskar, J., Fienga, A., Gastineau, M., & Manche, H. (2011b). La2010: A new orbital solution for the long-term motion of the Earth. *A&A*, *532*, A89. https://doi.org/10.1051/0004-6361/201116836

Laskar, J., Gastineau, M., Delisle, J. B., Farres, A., & Fienga, A. (2011c). Strong chaos induced by close encounters with Ceres and Vesta. *Astronomy & Astrophysics*, *532*, L4. https://doi.org/10.1051/0004-6361/201117504

Laskar, J., Joutel, F., & Boudin, F. (1993). Orbital, precessional, and insolation quantities for the Earth from -20 Myr to +10 Myr. *Astronomy and Astrophysics*, *270*, 522–533.

Laskar, J., Robutel, P., Joutel, F., Gastineau, M., Correia, A. C. M., & Levrard, B. (2004). A long-term numerical solution for the insolation quantities of the Earth. *Astronomy & Astrophysics*, *428*(1), 261–285. https://doi.org/10.1051/0004-6361:20041335

Lourens, L. J., Wehausen, R., & Brumsack, H. J. (2001). Geological constraints on tidal dissipation and dynamical ellipticity of the Earth over the past three million years. *Nature*, *409*(6823), 1029–1033. https://doi.org/10.1038/35059062

Ma, C., Meyers, S. R., & Sageman, B. B. (2017). Theory of chaotic orbital variations confirmed by Cretaceous geological evidence. *Nature*, *542*(7642), 468–470. https://doi.org/10.1038/nature21402

Marchegiano, M., & John, C. M. (2022). Disentangling the impact of global and regional climate changes during the Middle Eocene in the Hampshire Basin: New insights from carbonate clumped isotopes and Ostracod assemblages. *Paleoceanography and Paleoclimatology*, *37*(2), e2021PA004299. https://doi.org/10.1029/2021PA004299

Matthews, K. J., Maloney, K. T., Zahirovic, S., Williams, S. E., Seton, M., & Muller, R. D. (2016). Global plate boundary evolution and kinematics since the late Paleozoic. *Global and Planetary Change*, *146*, 226–250. https://doi.org/10.1016/j.gloplacha.2016.10.002

Meyers, S. R. (2014). Astrochron: An R package for astrochronology. Retrieved from http://cran.r-project.org/package=astrochron

Meyers, S. R., & Malinverno, A. (2018). Proterozoic Milankovitch cycles and the history of the solar system. *Proceedings of the National Academy of Sciences*, *115*(25), 6363–6368. https://doi.org/10.1073/pnas.1717689115

Milanković, M. (1941). Kanon der Erdbestrahlung und seine Anwendung auf das Eiszeitenproblem.

Müller, R. D., Cannon, J., Qin, X., Watson, R. J., Gurnis, M., Williams, S., et al. (2018). GPlates: Building a virtual Earth through deep time. *Geochemistry, Geophysics, Geosystems*, *19*(7), 2243–2261. https://doi.org/10.1029/2018GC007584

Newsam, C. (2016). *Calcareous nannoplankton evolution and the Paleogene greenhouse to icehouse climate-mode transition (PhD)*. London, UK: University College London (UCL). Retrieved from https://discovery.ucl.ac.uk/id/eprint/1541282/35/Cherry%20Newsam%20PhD%20Thesis.pdf

Norris, R. D., Wilson, P. A., Blum, P., Fehr, A., Agnini, C., Bornemann, A., et al. (2014). Expedition 342 summary. In R. D. Norris, P. A. Wilson, & P. Blum (Eds.), *The expedition 342 scientists, Proceedings of IODP*. Integrated Ocean Drilling Program. College Station, TX. https://doi.org/10.2204/iodp.proc.342.101.2014

Olsen, P. E., Laskar, J., Kent, D. V., Kinney, S. T., Reynolds, D. J., Sha, J., & Whiteside, J. H. (2019). Mapping solar system chaos with the geological Orrery. *Proceedings of the National Academy of Sciences*, *116*(22), 10664–10673. https://doi.org/10.1073/pnas.1813901116

Pälike, H. (2005). EARTH | orbital variation (including Milankovitch cycles). In R. C. Selley, L. R. M. Cocks, & I. R. Plimer (Eds.), *Encyclopedia of geology* (pp. 410–421). Elsevier.

Pälike, H. (2021a). OrbitalCalculations/AstroSolution: Zenodo v0.0.5 [Software][Dataset]. Zenodo. https://doi.org/10.5281/zenodo.5736415

Pälike, H. (2021b). OrbitalCalculations/hpnaff: V0.0.4 [Software][Dataset]. Zenodo. https://doi.org/10.5281/zenodo.5780014

Pälike, H., & Shackleton, N. J. (2000). Constraints on astronomical parameters from the geological record for the last 25 Myr. *Earth and Planetary Science Letters*, *182*(1), 1–14. https://doi.org/10.1016/S0012-821X(00)00229-6

Quinn, T. R., Tremaine, S., & Duncan, M. (1991). A three million year integration of the Earth's orbit. *The Astronomical Journal*, *101*, 2287. https://doi.org/10.1086/115850

Sinnesael, M., De Vleeschouwer, D., Zeeden, C., Batenburg, S. J., Da Silva, A. C., de Winter, N. J., et al. (2019). The cyclostratigraphy intercomparison project (CIP): Consistency, merits and pitfalls. *Earth-Science Reviews*, *199*, 102965. https://doi.org/10.1016/j.earscirev.2019.102965

Vahlenkamp, M., De Vleeschouwer, D., Batenburg, S. J., Edgar, K. M., Hanson, E., Martinez, M., et al. (2020). A lower to Middle Eocene astrochronology for the Mentelle Basin (Australia) and its implications for the geologic time scale. *Earth and Planetary Science Letters*, *529*, 115865. https://doi.org/10.1016/j.epsl.2019.115865

Vahlenkamp, M., Niezgodzki, I., De Vleeschouwer, D., Bickert, T., Harper, D., Kirtland Turner, S., et al. (2018). Astronomically paced changes in deep-water circulation in the Western North Atlantic during the middle Eocene. *Earth and Planetary Science Letters*, *484*, 329–340. https://doi.org/10.1016/j.epsl.2017.12.016

van der Ploeg, R., Cramwinckel, M. J., Kocken, I. J., Leutert, T. J., Bohaty, S. M., Fokkema, C. D., et al. (2023). North Atlantic surface ocean warming and salinization in response to middle Eocene greenhouse warming. *Science Advances*, *9*(4), eabq0110. https://doi.org/10.1126/sciadv.abq0110

Varadi, F., Runnegar, B., & Ghil, M. (2003). Successive refinements in long-term integrations of planetary orbits. *The Astrophysical Journal*, *592*(1), 620–630. https://doi.org/10.1086/375560

Waltham, D. (2015). Milankovitch Period uncertainties and their impact on cyclostratigraphy. *Journal of Sedimentary Research*, *85*(8), 990–998. https://doi.org/10.2110/jsr.2015.66

Westerhold, T., Marwan, N., Drury, A. J., Liebrand, D., Agnini, C., Anagnostou, E., et al. (2020). An astronomically dated record of Earth's climate and its predictability over the last 66 million years. *Science*, *369*(6509), 1383–1387. https://doi.org/10.1126/science.aba6853

Westerhold, T., & Röhl, U. (2013). Orbital pacing of Eocene climate during the middle Eocene climate optimum and the chron C19r event: Missing link found in the tropical Western Atlantic. *Geochemistry, Geophysics, Geosystems*, *14*(11), 4811–4825. https://doi.org/10.1002/ggge.20293

Westerhold, T., Rohl, U., Frederichs, T., Agnini, C., Raffi, I., Zachos, J. C., & Wilkens, R. H. (2017). Astronomical calibration of the Ypresian timescale: Implications for seafloor spreading rates and the chaotic behavior of the solar system? *Climate of the Past*, *13*(9), 1129–1152. https://doi.org/10.5194/cp-13-1129-2017

Westerhold, T., Rohl, U., Frederichs, T., Bohaty, S. M., & Zachos, J. C. (2015). Astronomical calibration of the geological timescale: Closing the middle Eocene gap. *Climate of the Past*, *11*(9), 1181–1195. https://doi.org/10.5194/cp-11-1181-2015

Westerhold, T., Rohl, U., Palike, H., Wilkens, R., Wilson, P. A., & Acton, G. (2014). Orbitally tuned timescale and astronomical forcing in the Middle Eocene to early Oligocene. *Climate of the Past*, *10*(3), 955–973. https://doi.org/10.5194/cp-10-955-2014

Zeebe, R. E. (2017). Numerical solutions for the orbital motion of the solar system over the past 100 Myr: Limits and new results. *The Astronomical Journal*, *154*(5), 193. https://doi.org/10.3847/1538-3881/aa8cce

Zeebe, R. E., & Lourens, L. J. (2019). Solar System chaos and the Paleocene–Eocene boundary age constrained by geology and astronomy. *Science*, *365*(6456), 926–929. https://doi.org/10.1126/science.aax0612

Zeebe, R. E., & Lourens, L. J. (2022). A deep-time dating tool for paleo-applications utilizing obliquity and precession cycles: The role of dynamical ellipticity and tidal dissipation. *Paleoceanography and Paleoclimatology*, *37*(2), e2021PA004349. https://doi.org/10.1029/2021PA004349

Zeeden, C., Hilgen, F. J., Husing, S. K., & Lourens, L. L. (2014). The Miocene astronomical time scale 9–12 Ma: New constraints on tidal dissipation and their implications for paleoclimatic investigations. *Paleoceanography*, *29*(4), 296–307. https://doi.org/10.1002/2014PA002615